Northumbria Research Link

Citation: Win Naung, Shine, Erfanian Nakhchi Toosi, Mahdi and Rahmati, Mohammad (2021) Prediction of flutter effects on transient flow structure and aeroelasticity of low-pressure turbine cascade using direct numerical simulations. Aerospace Science and Technology, 119. p. 107151. ISSN 1270-9638

Published by: Elsevier

URL: https://doi.org/10.1016/j.ast.2021.107151 <https://doi.org/10.1016/j.ast.2021.107151>

This version was downloaded from Northumbria Research Link: http://nrl.northumbria.ac.uk/id/eprint/47444/

Northumbria University has developed Northumbria Research Link (NRL) to enable users to access the University's research output. Copyright © and moral rights for items on NRL are retained by the individual author(s) and/or other copyright owners. Single copies of full items can be reproduced, displayed or performed, and given to third parties in any format or medium for personal research or study, educational, or not-for-profit purposes without prior permission or charge, provided the authors, title and full bibliographic details are given, as well as a hyperlink and/or URL to the original metadata page. The content must not be changed in any way. Full items must not be sold commercially in any format or medium without formal permission of the copyright holder. The full policy is available online: http://nrl.northumbria.ac.uk/policies.html

This document may differ from the final, published version of the research and has been made available online in accordance with publisher policies. To read and/or cite from the published version of the research, please visit the publisher's website (a subscription may be required.)

Northumbria University NEWCASTLE

CUSTOMER SERVICE EXCELLENCE CSE UniversityLibrary

Aerospace Science and Technology 119 (2021) 107151

Contents lists available at ScienceDirect

Aerospace Science and Technology

www.elsevier.com/locate/aescte

Prediction of flutter effects on transient flow structure and aeroelasticity of low-pressure turbine cascade using direct numerical simulations

Shine Win Naung, Mahdi Erfanian Nakhchi, Mohammad Rahmati *

Department of Mechanical and Construction Engineering, Faculty of Engineering and Environment, Northumbria University, Newcastle upon Tyne, NE1 8ST, United Kingdom

ARTICLE INFO

Article history:
Received 31 January 2021
Received in revised form 11 August 2021
Accepted 28 September 2021
Available online 7 October 2021
Communicated by Grigorios Dimitriadis

Keywords:
Direct numerical simulations
Low-pressure turbine
Wake interaction
Vortex generation
Separated shear layer

ABSTRACT

The aerodynamic characteristics of advanced low-pressure turbines (LPTs) could be affected by the interaction between the transitional and turbulent flow and the dynamic behaviour of the blades. Consequently, analysing the details of the interactions between the transient flow, blade vibrations and the flutter occurrence over the blades of LPTs are essential in order to enhance the aerodynamic efficiency of the modern LPTs. The distinctive feature of the present analysis is performing high-fidelity simulations based on a DNS approach employing a 3D blade model to investigate the flutter instabilities in a T106A turbine at various inter blade phase angles (IBPAs) at different Reynolds numbers. The impacts of the flutter on the transient flow structure are examined by using a direct numerical simulation method. The results show that at IBPA=0°, persistent patterns of vortex generation are detected with fluid flow mixing in the downward areas. For IBPA=180°, however, the recirculation generated by the upper blades proceeds toward the lower ones and interferes with the shedding from the trailing edge which impact the wake structure in the downstream regions significantly. A three-dimensional frequency domain model based on the harmonic balance method is also proposed in this study to investigate the capabilities and limitations of frequency domain methods in predicting aeroelasticity and details of flow structures in LPTs.

1. Introduction

Advanced Low-Pressure Turbines (LPTs) with high lift aerofoils are the key parts in the modern gas turbines and aeroengines [1]. They are distinctively manufactured to deliver high aerodynamic performances at low-pressure conditions, to regain exhaust energy while reducing the back pressure. The elevated blade loading, and the flow separation from the surface of the blade at different Reynolds numbers are common physical parameters of the state-of-the-art LPTs. The interactions between the unsteady fluid flow and the blade shape in LPTs could significantly influence the aerodynamic efficiency of the turbines. The highest efficiency of 93% can be achieved in LPTs by improving the geometry of the turbine's blades [2].

LPTs have around 30% of the total engine weight and decreasing their weights in aircraft engines and associated manufacturing expenses are key areas of research and development [3]. Designing high-lift turbine blades with high aerodynamic efficiency and lower number of blades is one of the solutions [4]. Nonetheless, this design could result in highly elevated per-stage loadings [5–7]. Moreover, the high aspect ratio of the blades could lead to aeroelastic instabilities like flutter [8] which can negatively affect the structural integrity of the blades [9–11].

Prediction of aeroelastic instabilities in turbomachinery blades is one of the main complex challenges in the design of aero-engines [12]. Many research studies were performed in the past years to develop accurate numerical methods for aeroelastic analysis [13–15]. Frequency-domain methods such as the harmonic solution method of He [16], and Rahmati et al. [19,20], are computationally very efficient, and they can predict aerodynamic and aeroelastic performances of various turbine blades at wide range of air flow velocities. In the numerical study of Rahmati et al. [17], a nonlinear frequency-domain method was developed to predict aerodynamic and aeroelasticity parameters of the blades of both a multistage compressor and turbine. It was observed that a multi-row simulation can predict the flutter more precisely compared

---

* Corresponding author.
E-mail address: mohammad.rahmati@northumbria.ac.uk (M. Rahmati).

https://doi.org/10.1016/j.ast.2021.107151

to the basic isolated blade-row cases [18]. Recently, frequency-domain methods were also applied to the analysis of wind turbines [19,20]. In a numerical study of Shine et al. [21], they employed a nonlinear frequency-domain approach to investigate the aeroelastic performances of wind turbines considering different sources of flow unsteadiness. They also applied this method to the aeromechanic simulations of a full wind turbine system including a tower [22]. They found that the proposed model can not only predict the aerodynamic flow-filed and aeroelasticity of wind turbines accurately but also decrease the computational costs substantially compared to the traditional time-domain methods.

The current available aeroelastic solvers are built upon the Unsteady Reynolds Averaged Navier–Stokes (URANS) models. However, the methods based on URANS models are not able to accurately calculate the performance of the transient flows, particularly in the separated regions, because of the insufficiency of the existing turbulence modelling techniques [23–25]. So, the flow details and precision would not be achieved by the URANS models in the presence of the flow separation, pressure fluctuations and vortex generations, which are common phenomena in modern LPTs used in aeroengines. The current aeroelasticity models utilized in the aerospace industries primarily concentrate on aeroelastic factors such as the aerodynamic damping and ignore the complicated unsteady flow behaviour happening through fluid-structure interactions (FSIs). Hence, in order to better examine the physical details of the interaction between the transitional flow field and the flutter instabilities over the blade, high-fidelity computational models are necessary. Recently, Nakhchi et al. [26] performed a direct numerical simulation (DNS) over an oscillating low-pressure turbine blade using the Spectral/hp element method and predicted flow structures due to the oscillating blade. In another numerical study of Shine et al. [27], they employed a DNS method to evaluate the interactions amongst the transient flows and the blade oscillations in an LPT. Both studies found that the blade oscillations have a major impact on the flow separation and vortex generation. However, these methods are based on a quasi-3D model with a periodic boundary condition in the span-wise direction. In an experimental and computational study conducted by Huang et al. [28], they investigated unsteady flows in a linear turbine cascade under oscillations. Their study shows the 3D behaviours of the flow due to the bending mode of the blade structure and a need to use a fully 3D solution method to analyse the vortex generation and flow structures associated with the vibration.

The main goal of this study is to investigate the flutter instabilities of the 3D blade structure in low-pressure turbines of the aircraft engines. A high-fidelity computational method is employed by considering the flow unsteadiness related to the fluid-structure interactions of a 3D blade model. Based on the above literature review and to the authors' knowledge, most previous studies in the field of LPTs have only concentrated on the transitional flow behaviour and separation point at the blade mid-span of modern LPTs. Therefore, it motivates the authors to develop a 3D numerical model, based on a high-fidelity DNS method, to examine the impacts of the oscillating LPT blade structure on the vortex generation and the aeroelastic performance of the turbine at different Reynolds numbers and inter blade phase angles (IBPAs). The values of the IBPAs are selected in a manner to completely analyse the in-phase and out-of-phase circumstances among two adjacent blades. The present study investigates the mechanisms of the interactions between the aerodynamic flows and the turbine blade's structure in advanced LPTs. The simulations are performed using the DNS based time-domain procedure and the harmonic balance method. The present paper can help the designers of LPT blades in aeroengines to predict the aerodynamic behaviour of the turbine blades under realistic physical conditions.

2. Physical description

2.1. Geometry of the turbine blade

In the present study, T106A turbine cascade, which is popular for the study of complex flow through modern low-pressure turbines in aeroengines, is chosen for the DNS simulations. Based on the available experiment and its data [29], various numerical studies [30–37] were performed to validate the different numerical models and to predict the flow structures inside this turbine numerically. In order to highlight the effect of the blade oscillation on the flow behaviour compared to the previously studied stationary blade cases and to show the advantages of the present work in predicting them, similar flow and geometrical parameters were selected. The blades aspect-ratio and pitch-chord ratio are selected as 1.760 and 0.799, respectively. The Reynolds number employed in the aforementioned experiment and numerical studies is 5.1×10^4. As discussed by Opoka et al. [38], the Reynolds numbers of a low pressure turbine blade can be around 5×10^4 at a high altitude in small jet applications. Moreover, the unsteady effects of a low-pressure turbine were measured at the Reynolds number between 2.5×10^4 and 1×10^5 in [39]. Therefore, the Reynolds number, based on the chord length of the blade, is varied from 2.5×10^4 to 7.5×10^4 with the velocity inlet angle α=45.5° are found to be appropriate for the present analysis to not only validate the numerical model but also analyse the effects of Reynolds numbers. The details of geometrical parameters of the LPT blade are presented in Fig. 1. Titanium Alloy is selected as the blade material with a density of 4620 kg/m^3, Young's modulus of 9.60×10^{10} Pa and Poisson's ratio of 0.36. Performing a modal analysis using the selected material, the first natural frequency is estimated to be 250 Hz. In a modal analysis of a low-pressure turbine blade performed by Antony et al. [40], the first natural frequency using a conventional titanium material is found to be as high as 455 Hz. Besides, in an experimental study of Forbes et al. [41], it is also found that the first natural frequency of a stationary blade of a gas turbine is approximately 117 Hz and that of a rotating blade is around 760 Hz. Furthermore, the frequencies ranging from 100 Hz to 400 Hz are also applied to the simulations of the low-pressure turbine blade at low Reynolds numbers in [42]. Therefore, it is determined that the frequency of 250 Hz, which corresponds to a dimensionless reduced frequency of 1.5, is suitable for this analysis and consistent with the previous research studies. The time-averaged pressure coefficients along the mid-section of the LPT blades were evaluated and compared with the experiments in the next sections. The blade's suction and pressure surfaces, the hub and the shroud of the LPT passage are considered as no slip walls, and periodic BCs are used in the pitch-wise directions. The pressure-outlet boundary condition is also implemented at the outer surface of the domain. Prior to the CFD analysis, a modal analysis is performed to evaluate the natural oscillation frequencies of the blade for the aeroelastic behaviour of the turbine. The first natural frequency is utilized for the precise prediction of the effect of the blade oscillation in numerical simulations of LPTs.

2.2. Computational model

A three-dimensional computational domain including the hub and shroud is used in this study to simulate a 3D model. The flow inlet and outlet are located $2C_{ax}$ from the leading edge and the trailing edge of the blade, respectively, where C_{ax} is the axial chord length. In the pitch-wise direction, a translational periodic boundary condition is applied to represent straight blade rows of a linear turbine cascade. The pitch length between two consecutive blade rows is $0.9306C_{ax}$. The span of the blade is considered to be $2.5C_{ax}$ to investigate the flow structures associated with the 3D

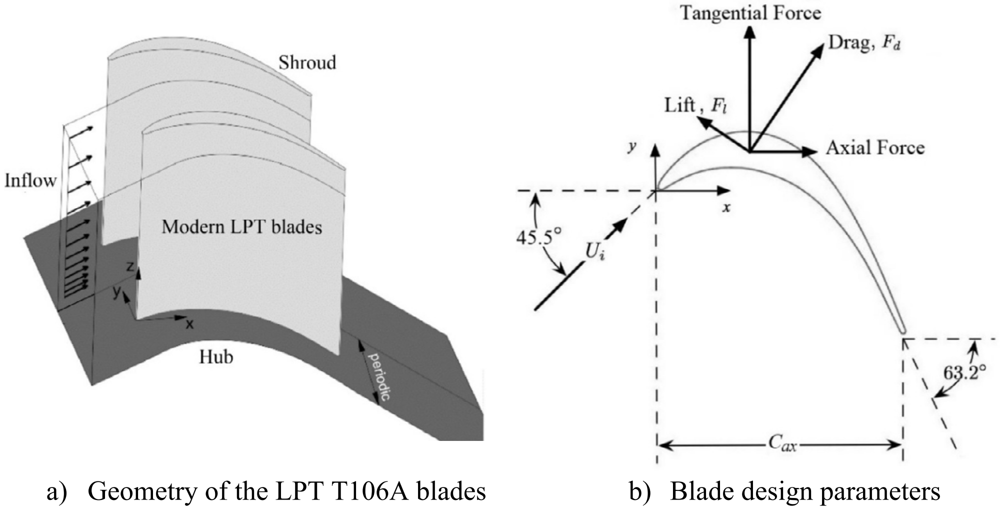

Fig. 1. Geometrical and physical parameters of the LPT T106A blade.

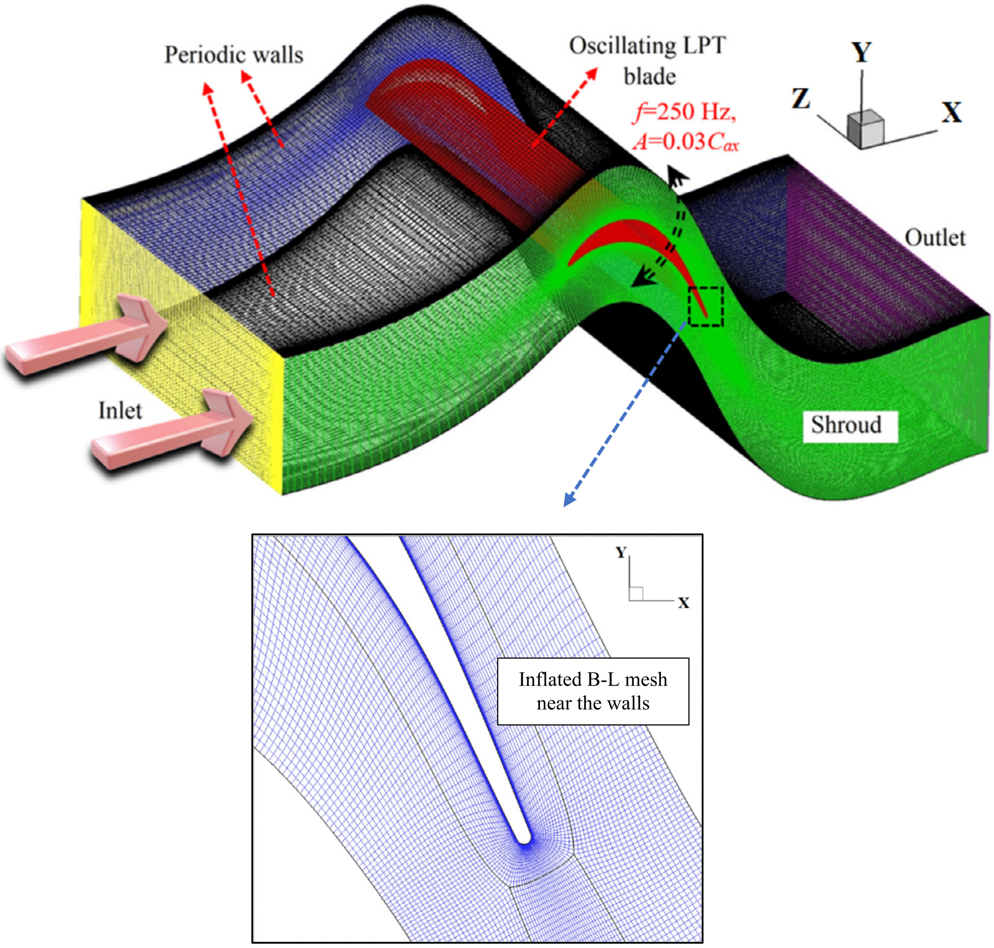

Fig. 2. Details of the representative computational domain and mesh of the LPT blade.

blade model and 3D vibration mode. The details of the generated computational domain and grid are presented in Fig. 2. The mesh is generated based on an O4H topology using a structured mesh generator. The grid point distributions in the stream-wise direction and the pitch-wise direction in a single domain are 1028 and 140, respectively. 115 layers are distributed along the span of the blade in the span-wise direction. A single domain is used for the 0° IBPA case. In the case of 180° IBPA, another identical domain is added on the top of the reference domain and an internal interface using the general connection type is employed to connect the two domains and to transfer the flow data across the interface.

It is understood that a sufficient mesh resolution is crucial for a DNS simulation to resolve necessary flow details. Various mesh resolutions are being tested including 4.5×10^6 (coarsest grid) and 18×10^6 (finest grid) for this study. The grid point distribution for the finest grid is similar to the mesh resolution of Wissink et al. [33] (18×10^6) and that of Michelassi et al. [37] (17×10^6), and it was found that the finest grid provides better prediction of the unsteady pressure distributions and downstream wake which are comparable to the aforementioned reference studies. The difference between the present study and those of Wissink et al. [33] and Michelassi et al. [37] is the inflow condition as a steady inflow is only considered in the present study whereas inflow wakes are generated in the latter ones. Therefore, a fine mesh is not necessary in the inlet block for the present simulation, that leads to an optimum mesh size of 16.5×10^6 grid points. It should also be noted that the present simulation is the continuation of the authors' previous work [27] in which 13.5×10^6 grid points are employed for a quasi-3D model.

2.3. Computational methodology

In the first step, direct numerical simulations have been performed over the stationary LPT blade for the comparison with the available experimental and numerical data in the literature. Then, oscillations of the blade are implemented by defining specific vibration frequency and amplitude along the blade of the turbine passage. The vibration frequency is estimated based on the first natural vibration frequency of the T106 blade obtained by conducting the modal analysis in a structure solver using a finite element method. The effects of the vibrations on the flutter instabilities over the blades and the fluctuations of vortex generation in the separated shatter layer will be investigated under the turbulent/transitional flow regimes. Two computation methods such as the time-domain method and harmonic balance technique have been utilized for the simulations to capture the strong recirculations and transient flow behaviour in the separation bubble and also in the wake region of the modern LPT blade.

The unsteady Navier-Stokes (N-S) equation in general three-dimensional form, and in the cartesian coordinates can be defined by:

$$\frac{\partial}{\partial t}\int_{\Omega} U d\Omega + \int_{S} \vec{F}_I . d\vec{S} + \int_{S} \vec{F}_V . d\vec{S} = \int_{\Omega} S_T d\Omega \tag{1a}$$

In this equation, Ω and S are the volume and surface, respectively. U is the vector of a conservative variable, and it can be defined as:

$$U = [\rho, \rho v_1, \rho v_2, \rho v_3, \rho E]^T \tag{1b}$$

$\vec{F}_I$ and $\vec{F}_V$ are the inviscid and viscous flux terms, respectively. They can be expressed as:

$$\vec{F}_I = [\rho v_i, \rho v_1 v_i + p, \rho v_2 v_i + p, \rho v_3 v_i + p, (\rho E + p) v_i]^T \tag{1c}$$

$$\vec{F}_V = \left[0, \tau_{i1}, \tau_{i2}, \tau_{i3}, q_i + v_j \tau_{ij}\right]^T \tag{1d}$$

The source term (S_T) can be defined as:

$$S_T = \left[0, \rho f_{e1}, \rho f_{e2}, \rho f_{e3}, W_f\right]^T \tag{1e}$$

where f_{e1} to f_{e3} are the components of the external forces in the governing equation (1a), and $W_f = \rho \vec{f}_e . \vec{v}$ is the work done by the external forces.

Eq. (1) can be expressed in the simple form, as:

$$\frac{\partial}{\partial t}(U) = R(U) \tag{2}$$

Where R is the lumped residuals and the source terms of the N-S equation.

In this paper, direct numerical simulation is approached by solving the incompressible N-S equations directly without modelling turbulence by means of turbulence models. A three-dimensional pressure-based incompressible finite volume solver is used to solve the N-S equations in this study. A pseudo-time marching method is employed to solve the steady-state equations which is then used as an initial condition for the unsteady solution. A cell centred finite volume method is applied to the discretization of the N-S equations. The mass and momentum equations are integrated over each control volume, and Gauss' Theorem is used to for the conversion of volume integrals to surface integrals as expressed below, so that the gradients φ can be evaluated on the cell faces.

$$\vec{\nabla}\varphi = \frac{1}{\Omega}\int \vec{\nabla}\varphi d\Omega = \frac{1}{\Omega}\varphi d\vec{s} \tag{3}$$

A 2nd order bounded central differencing scheme is employed for the spatial discretization, and it is expressed as:

$$\varphi_f = \varphi_N + \beta \vec{\nabla}\varphi . \Delta\vec{n} \tag{4}$$

where φ_f and φ_N are the values at the cell face and at the node of a neighbouring cell. $\vec{n}$ is the vector from the neighbouring node to the cell face. With a central differencing scheme, β is set to 1. The SIMPLE algorithm is used for the pressure-coupling scheme.

A harmonic balance method is also implemented in the present study to investigate its capability on predicting unsteady flow structures due to the effect of the blade flutter. Using this method, the transient flow variables, U, can be modelled based on a Fourier series for a prescribed fundamental frequency, ω, and a specified number of harmonics, q, as expressed in Eq. (5).

$$U = \overline{U} + \sum_{q=1}^{Q}\left[A_q \sin(q\omega t) + B_q \cos(q\omega t)\right] \tag{5}$$

where $\overline{U}$, A_q, and B_q are Fourier coefficients of the conservative variables. Substituting Eq. (5) into Eq. (2) produces the following equations.

$$\omega \sum_{q=1}^{Q}\left[q A_q \cos(q\omega t) - q B_q \sin(q\omega t)\right] = R \tag{6}$$

With a harmonic balance method, an unsteady period of the blade vibration cycle can be divided into $N = (2q+1)$ time levels, and the system of nonlinear equations coupling all N time levels are solved iteratively. A spectral approximation approach is employed to evaluate the time derivatives in this method.

As a blade vibration is involved, the mesh deformation becomes an important treatment for the simulation. A wall boundary of the blade is deformed as expressed below:

$$\delta(t) = \bar{\delta} + \delta_A cos(\omega t) \tag{7}$$

where $\bar{\delta}$ and δ_A are the average and amplitude of the blade deformation. The mesh deformation treatment is determined by the displacement diffusion mesh deformation model. With this mode, the displacements specified on the boundary nodes of the blade are diffused to other grid points by solving the following equation.

$$\nabla . \left(\Gamma_{disp} \nabla \delta\right) = 0 \tag{8}$$

In this equation, δ is the displacement with respect to the previous grid location and Γ_{disp} is the mesh stiffness, which controls the node movements. In this study, the mesh stiffness is increased near the small volumes. The benefit of expanding the stiffness near small cells is that overall mesh quality is improved by absorbing more mesh motion in larger control volumes. The mesh stiffness

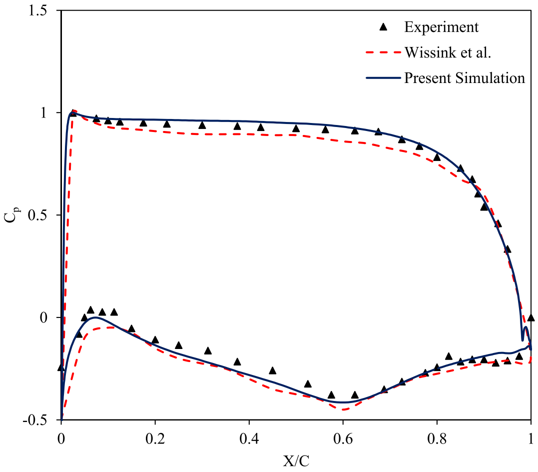

Fig. 3. Validation of the time-averaged *Cp* with the experiment and the reference simulation over a stationary blade.

value is determined by the following equation and applied in the displacement diffusion equation, expressed in Eq. (8).

$$\Gamma_{disp} = \left(\frac{L_{ref}}{L}\right)^{C_{stiff}} = 0 \tag{9}$$

In this equation, the stiffness model exponent, C_{stiff}, determines the rate of the increment of the stiffness value, which increases as the size of the control volume, L, decreases. L_{ref} is the reference control volume.

To achieve a high resolution of the unsteady flow structures, the flow should move only a fraction of the length of the cell h with a fluid velocity u in each step of the computation. Therefore, the time-step size Δt used in the computation must be very small, and it can be determined based on the following equation.

$$CFL = u\Delta t/h \tag{10}$$

The CFL number must be kept below unity to obtain a very small time-step and to avoid the simulation divergency.

3. Results and discussions

3.1. Validations

Prior to investigating the impact of flutter instabilities on the transient flow structure over the LPT blades, it is necessary to validate the results from the present simulation by comparing them to the experimental and numerical data available in the literature. For this purpose, the time-averaged pressure coefficient profiles at midsection of the blade are evaluated. The pressure coefficient can be defined as $C_p = (p_w - p_{ref}) / (p_{t-in} - p_{ref})$, where p_w, p_{ref}, and p_{t-in} are the static wall pressure, reference outflow pressure, and total inflow pressure. Fig. 3 shows the validation of the pressure coefficient from the present numerical study with the experimental data and DNS results of Wissink et al. [33] for stationary turbine blades without considering the realistic oscillations. It is observed that the numerical results of the present study are in excellent agreement with previous results available in the literature for stationary LPT blades.

The time-averaged wake-loss profile can be calculated as $\omega_u = (p_{t-in} - p_t) / (p_{t-in} - p_{ref})$ where p_t is the total pressure which is calculated at 40% of the chord in the downstream of the blade. The results are compared with the experimental data and the previous numerical results of Michelassi et al. [36] in Fig. 4. The comparison reveals that the proposed three-dimensional model is able to capture the wake-loss profile correctly. Therefore, it can be deduced that the mesh utilized for the numerical simulations is appropriate enough to capture the flow structures subject to blade oscillations.

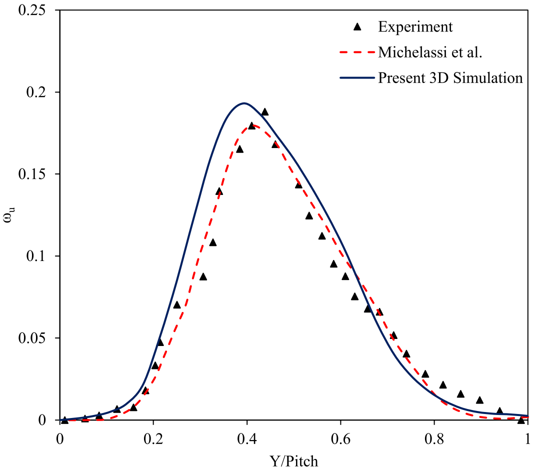

Fig. 4. Validation of the wake profile with the experimental and the numerical data over a stationary blade.

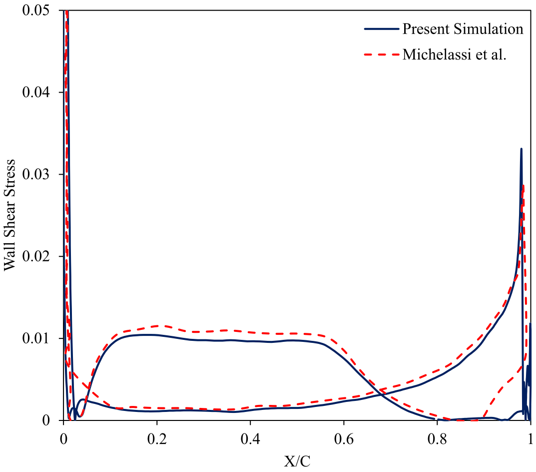

Fig. 5. Validation of the WSS with the experimental data (stationary blade) at Re=5.1×10^4.

Along with the Cp and wake profile variations, the wall shear stress (WSS) values on the suction surface and the pressure surface of the turbine blade are evaluated. Fig. 5 shows the comparison of WSS values between the present work and the numerical results of Michelassi et al. [36]. It can be seen that a close agreement was observed between the results of the present study and the previous work. As good agreements were obtained between the numerical results and the reference data available in the literature, it can now be concluded that the proposed numerical model is trustworthy and can be utilized for further simulations.

The unsteady pressure coefficient obtained in the present work is compared with the previous study of Nakhchi et al. [26] over the vibrating T106 blade in Table 1. Good agreement is observed between the results of the present study and the previous one over the vibrating LPT blade. The results are provided for different axial sections over the LPT blade on both the suction side and pressure side of the blade.

The main aim of this study is to investigate the details of the transient flow structures because of the interactions of the flow with the turbine blades. It is essential to develop a high-fidelity numerical model to capture the details of the vortex generations

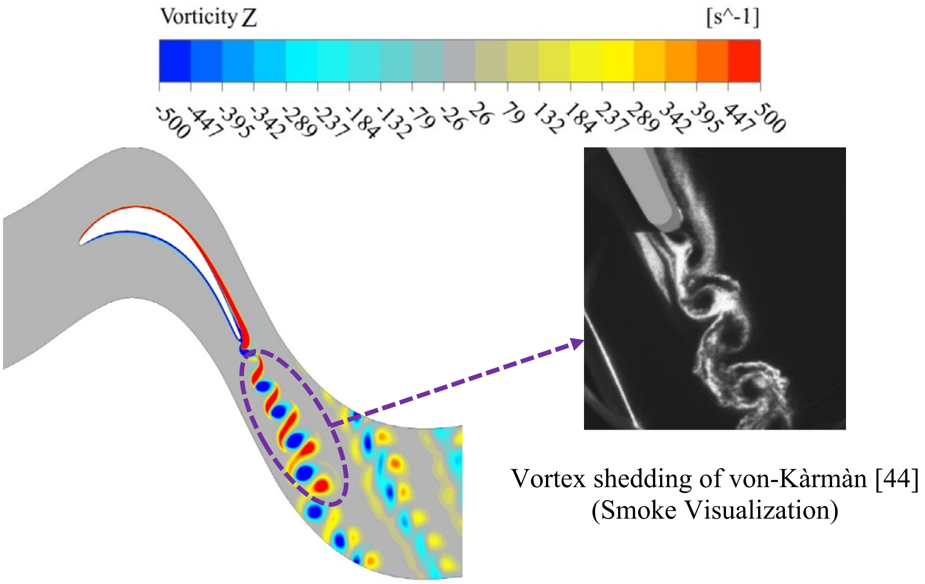

a) Vorticity (z) at T_1^*

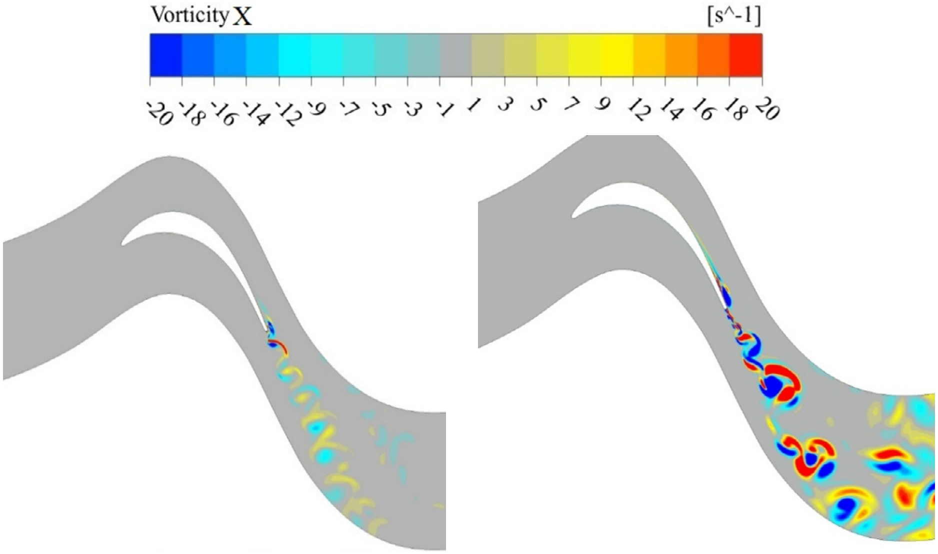

b) Vorticity (x) at T_1^*

c) Vorticity (x) at T_2^*

Fig. 6. Instantaneous vorticity contours in the X and Z directions at 50% span at Re=5.1 × 10^4. (For interpretation of the colours in the figure(s), the reader is referred to the web version of this article.)

Table 1
Validation of the unsteady pressure coefficient over the vibrating LPT blade with the numerical results of Nakhchi et al. [26].

X/C	Pressure surface		Suction surface	
	Present study	Nakhchi [26]	Present study	Nakhchi [26]
0.1	1.012	1.065	0.709	0.711
0.3	1.215	1.210	0.518	0.520
0.5	1.279	1.275	0.289	0.289
0.7	1.220	1.227	0.082	0.081
0.9	0.829	0.832	0.316	0.318

and fluctuations in the flow structure over the blades due to the oscillations. Fig. 6 shows the instantaneous vorticity contours in the X and Z directions at the mid-section of the blade (50% span) at 2 equally spaced times. It can be seen that the flow separation is occurred on the suction side of the blade prior to the trailing edge vortex shedding. The results show that the flow stays laminar without detachment on the pressure surface of the turbine

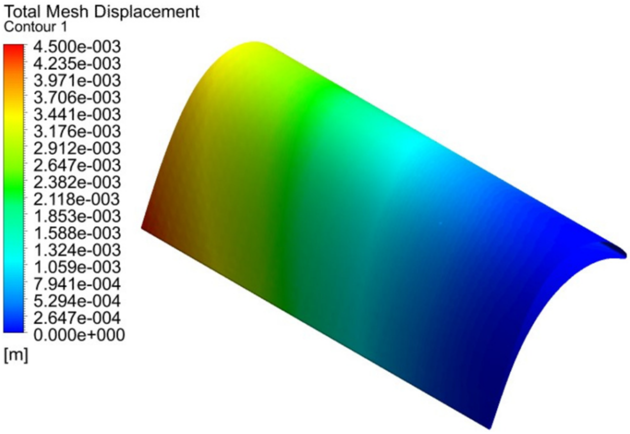

Fig. 7. Total mesh displacement of the LPT blade at the first vibration mode.

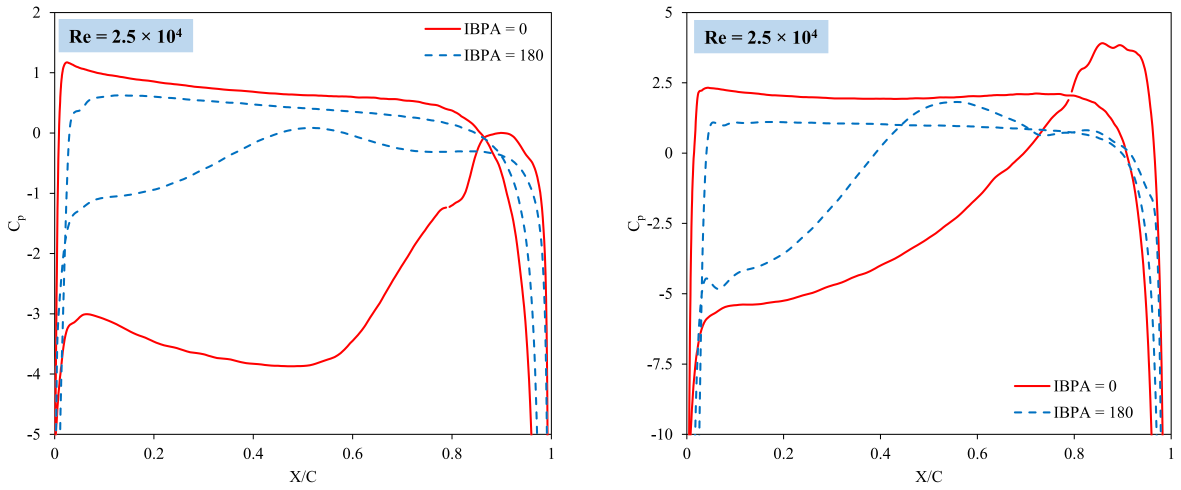

a) Re=2.5×10^4, 50% Span b) Re=2.5×10^4, 90% Span

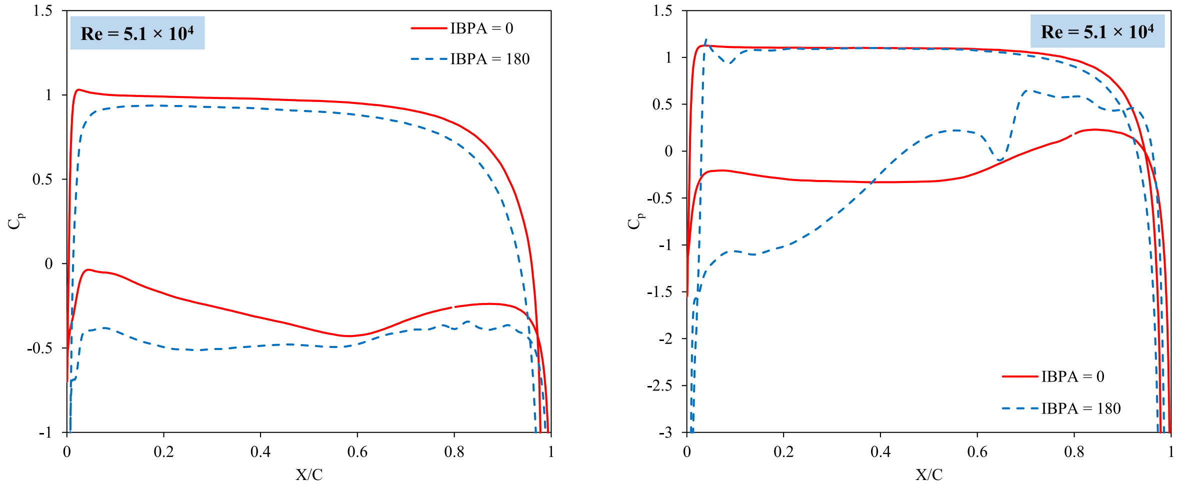

c) Re=5.1×10^4, 50% Span d) Re=5.1×10^4, 90% Span

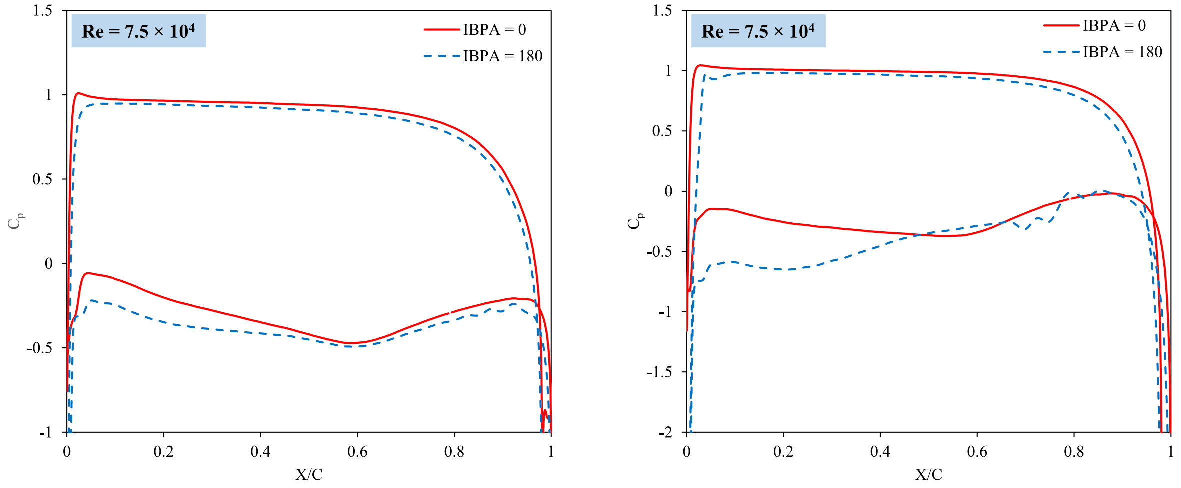

e) Re=7.5×10^4, 50% Span f) Re=7.5×10^4, 90% Span

Fig. 8. C_p comparison between IBPA=0° and 180° at different blade sections at different Re numbers.

blade. Von-Karman vortex shedding near the trailing edge of the blade, which is known as Karman vortex, is dominant within the early time steps. Similar behaviour is also detected in experimental visualisations [43,44]. The separated shear layers are generated by moving toward the solution time. The rolling up and shattering down of the detached shear layers arise because of the Kelvin-Helmholtz instabilities leading to the onset of transition from laminar to turbulence flow behind the trailing edge. After specific time steps, the flow is reattached to the surface of the blade and generates recirculations of the vortex structures in the downstream area

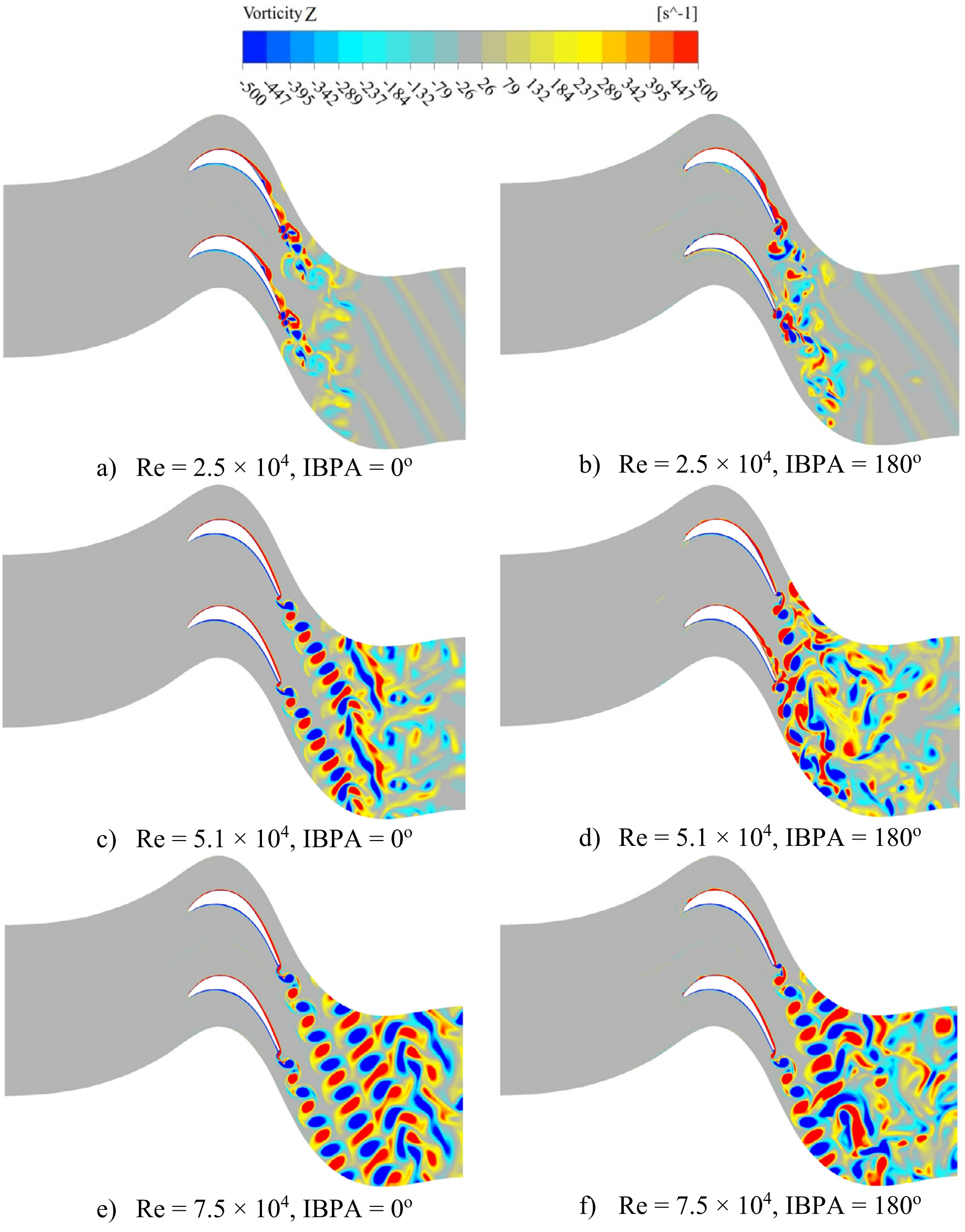

a) Re = 2.5 × 10^4, IBPA = 0°
b) Re = 2.5 × 10^4, IBPA = 180°
c) Re = 5.1 × 10^4, IBPA = 0°
d) Re = 5.1 × 10^4, IBPA = 180°
e) Re = 7.5 × 10^4, IBPA = 0°
f) Re = 7.5 × 10^4, IBPA = 180°

Fig. 9. Vorticity contours at different Reynolds number and IBPAs.

of the blade. These recirculating flows cause strong unsteadiness and fluctuations in the wake region. Consequently, the high-fidelity numerical model which is employed in the present study is able to capture the details of the transitional flow structure over the turbine blades which could be utilized for the design process of low-pressure turbines.

The modal analysis showed that the first natural frequency of the T016A blade is 250 Hz. This vibration frequency is employed to predict the flutter instabilities over advanced low-pressure turbine blade.

Fig. 7 depicts the total mesh displacement of the first vibration mode shape of the T106A blade. In an experimental and numerical study of a low-pressure turbine cascade performed by Huang et al. [28] and a numerical study of Rahmati et al. [18], a vibration amplitude of 3%C_{ax} was specified at the tip of the blade, where C_{ax} is the axial chord length. With the purpose of analysing the effect of a relatively high amplitude, a maximum vibration amplitude of 3%C_{ax} is also considered in this study. The authors previously spec-

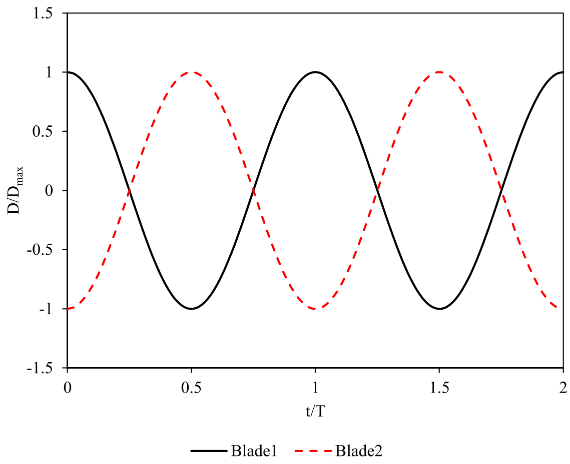

Fig. 10. Blade displacements over two vibration cycles.

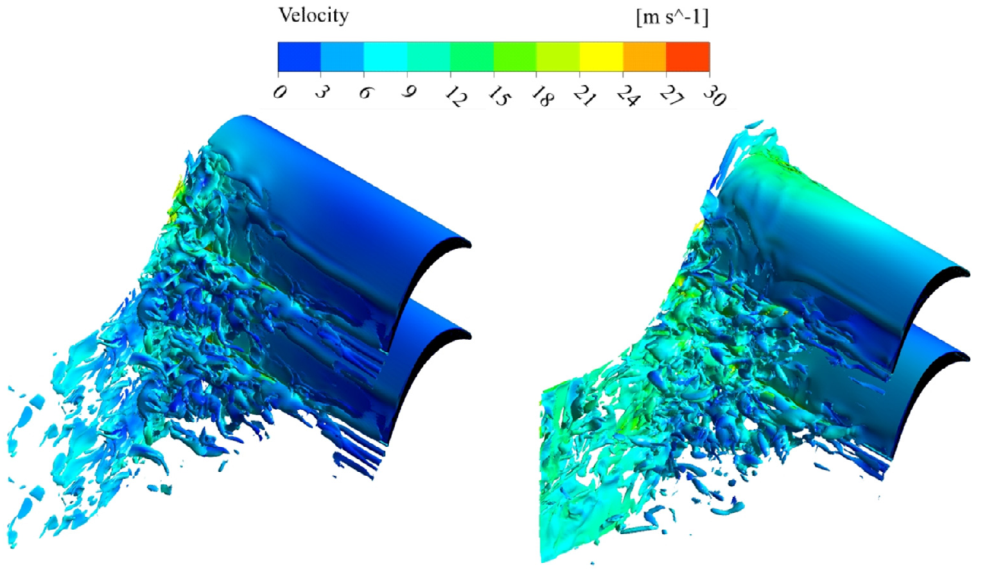

a) Re = 2.5 × 10^4, IBPA = 0°

b) Re = 2.5 × 10^4, IBPA = 180°

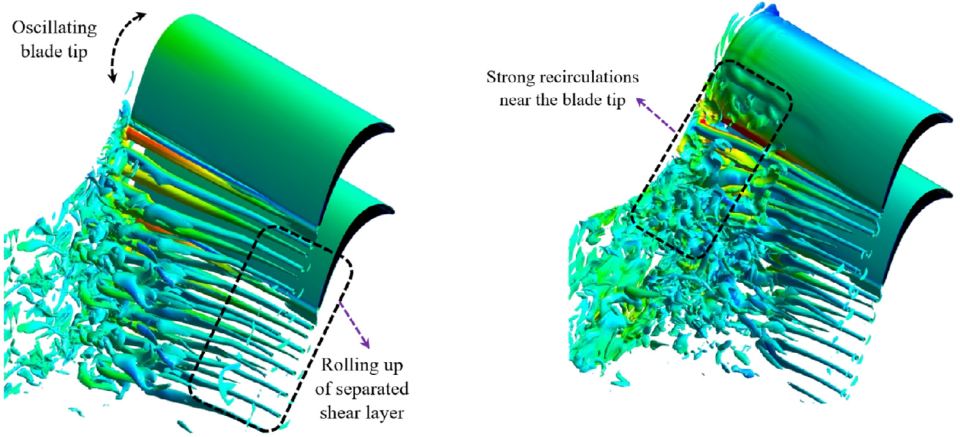

c) Re = 5.1 × 10^4, IBPA = 0°

d) Re = 5.1 × 10^4, IBPA = 180°

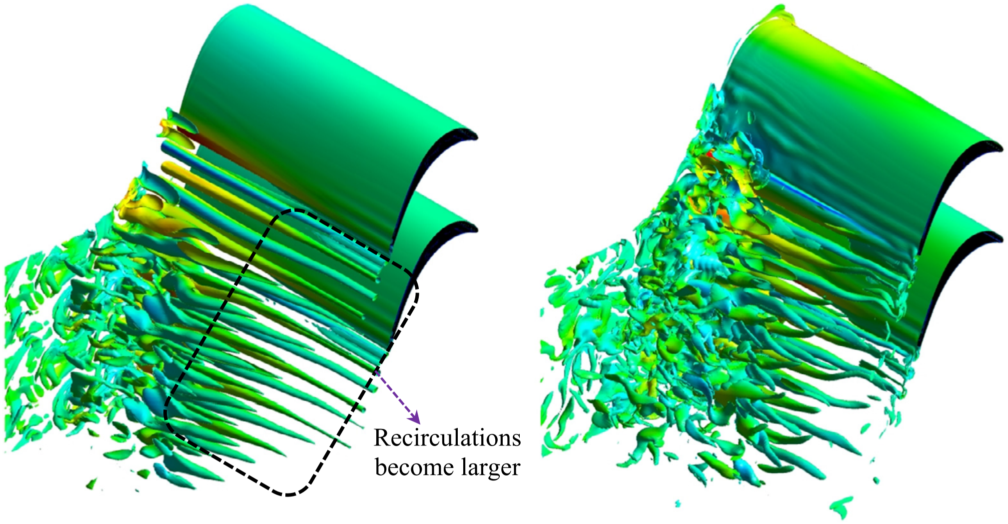

e) Re = 7.5 × 10^4, IBPA = 0°

f) Re = 7.5 × 10^4, IBPA = 180°

Fig. 11. Iso-surfaces of vorticity at different Reynolds number and IBPAs.

ified an amplitude of 1%C_{ax} in the quasi-3D models representing the mid-section of the blade [26,27]. By specifying a 3%C_{ax} amplitude at the tip of the blade, the amplitude at the mid-span section of the blade is also approximately 1%C_{ax}, which is commonly used in most studies. Two different IBPAs of 0° and 180° are selected for the present study. Analysing the effect of the in-phase and out-of-

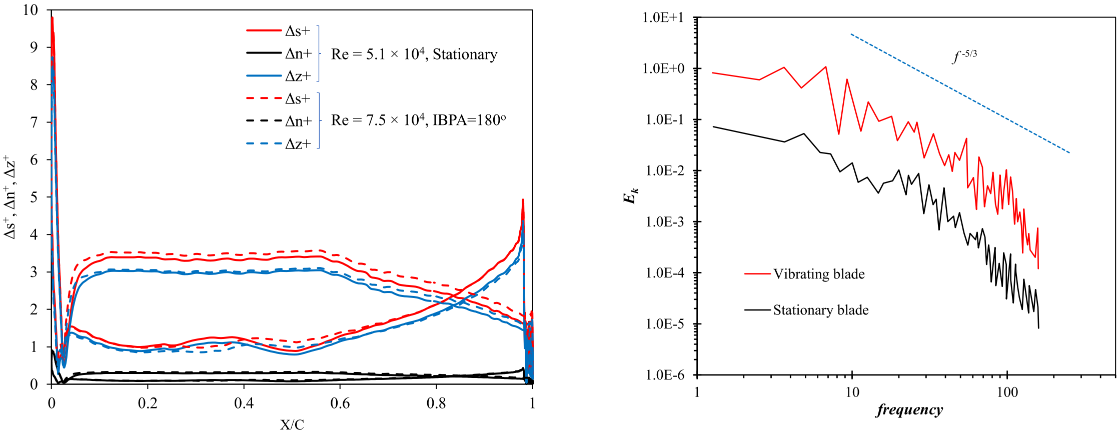

a) Near wall mesh resolution

b) Power spectra

Fig. 12. Near wall mesh resolution and power spectra of the kinetic energy from the stationary blade case and the vibrating blade case at Re = 7.5 × 10^4 and IBPA = 180°.

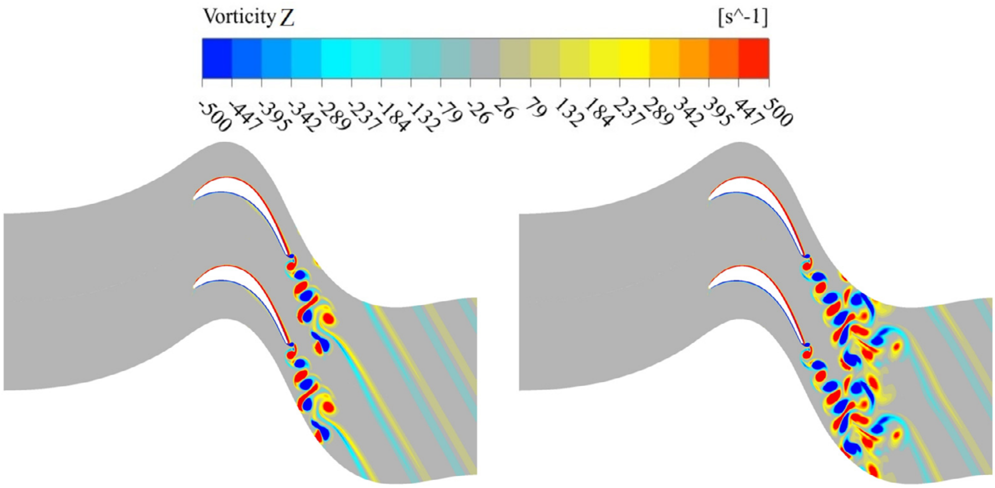

a) After 5 Vibration Periods

b) After 10 Vibration Periods

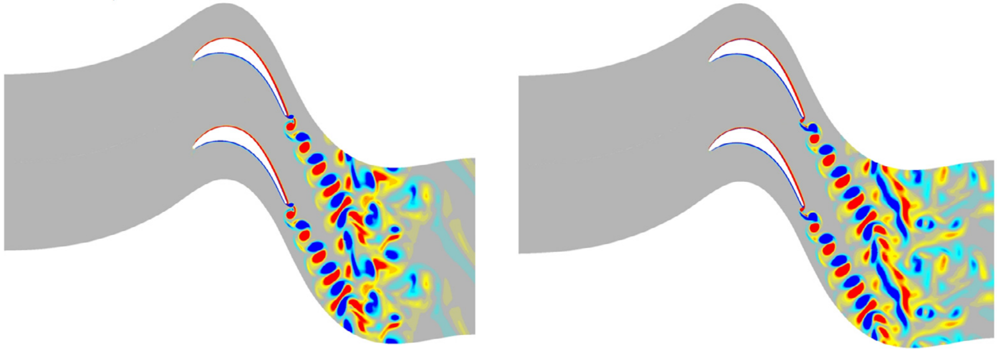

c) After 15 Vibration Periods

d) After 20 Vibration Periods

Fig. 13. The effects of vibration periods on the vortex generation contours over the oscillating blade with IBPA=0°.

phase vibration between two consecutive blade rows will provide a detailed understanding of the flow physics for the design of LPT blades in advanced aeroengines.

Fig. 8 shows the time-average pressure coefficient (C_p) variations over the suction and pressure sides of the LPT blade for both vibrating cases with IBPA=0° and IBPA=180° at different Reynolds numbers. The results are provided for different span sections. It can be observed that the pressure variations over the blade surfaces are primarily influenced by the blade oscillation with various IBPAs. At IBPA=180°, there are substantial impacts on the blade because of the variations in the pitch length among the oscillating turbine blades. The influence is considerably higher in the blade tip region behind the shroud due to the stronger oscillations, especially when the flow over one blade is disrupted by those of the nearby blades. Similar flow behaviour is detected at IBPA=0^0. In terms of the effect of Reynold number on the pressure distributions, significant differences are seen between the two IBPA cases at Re = 2.5 × 10^4. Due to a lower inflow speed at a low Reynolds number, the flow separates early on the suction surface, compared to other Reynolds number, and the recirculation of the separated shear layer occurs in the separation zone. The interaction between the separated flow at a relatively lower fluid velocity and the blade

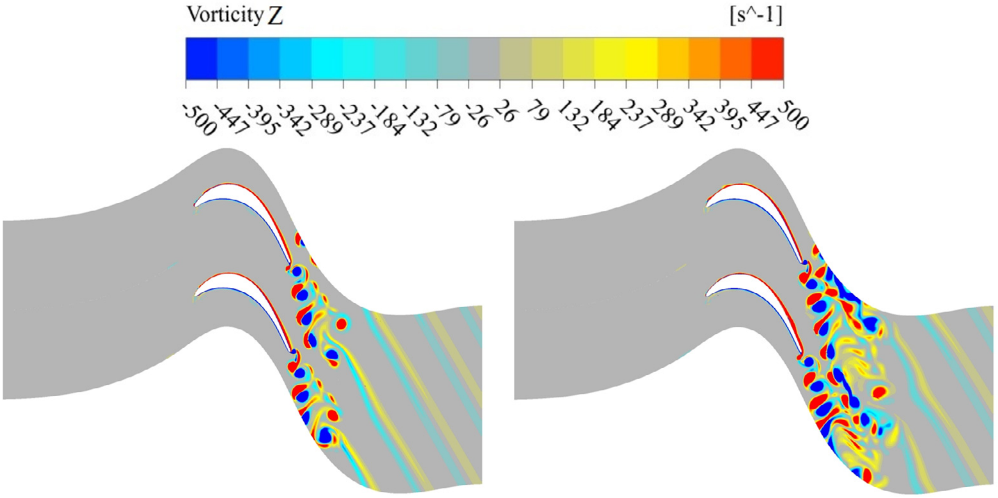

a) After 5 Vibration Periods

b) After 10 Vibration Periods

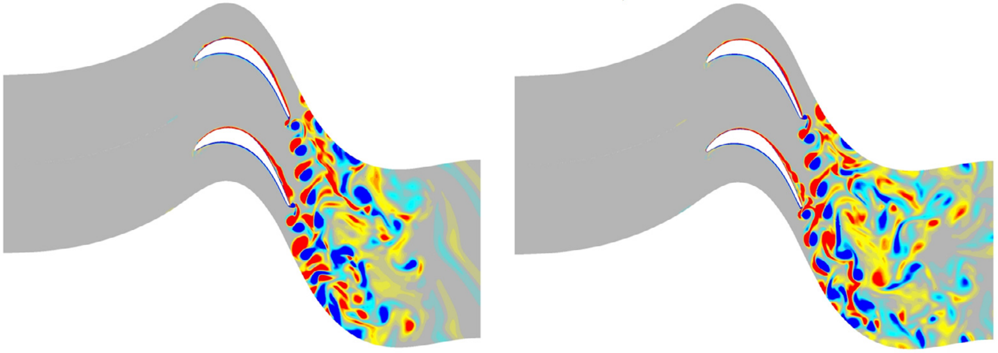

c) After 15 Vibration Periods

d) After 20 Vibration Periods

Fig. 14. The effects of vibration periods on the vortex generation contours over the oscillating blade with IBPA=180°.

oscillation enhances the flow unsteadiness. This unsteadiness is further amplified when the blades are vibrating at an IBPA of 180°. Raising the Reynolds number to 5.1×10^4 reduces these differences in the blade inner region. The resistance of the boundary layer separation is increased when raising the Reynolds number. However, in the blade outer region where the vibration amplitude is relatively high, the flow separation and the vortex generation are still stronger. Consequently, it is observed that the differences between the two IBPA cases are higher at 90% span. Furthermore, the out-of-phase vibration mode at an IBPA of 180° produces more disturbances to the unsteady flow and further complicates the formation the flow structures. It is also noted that the boundary layer separation is reduced by increasing the Reynolds number to 7.5×10^4 that, at the same time, decreases the flow unsteadiness caused by the separated shear layer, and thereby reducing the differences in pressure distribution at IBPA=0° and 180°.

The effect of IBPA and Reynolds number on the spanwise vorticity production is presented in Fig. 9. The results are extracted at the mid-span section of the blade. The flow separation and rolling up of the separated shear layers are seen on the suction surface of the blade when the Reynolds number is 2.5×10^4. At Re $= 5.1 \times 10^4$, the flow unsteadiness and turbulence in the wake region is much higher in the case of IBPA=180° compared to that of 0°. When Re $= 7.5 \times 10^4$, the flow structures and vortex shedding from the trailing edge of the blade are similar in both IBPA cases. However, the mixing of flow structures is observed in the far downstream region at IBPA=180°. It is also observed that the size of flow structures and recirculation becomes larger when raising Reynolds number. Moreover, the structure of the vorticity in the downstream region is significantly dependent on the IBPA. The results illustrate that the flow disturbance and fluctuations in the vortex shedding process become noticeable by increasing IBPA from 0° to 180°. This is due to the blades moving out of phase to each other. The phase-shift between the two adjacent blades can be seen in Fig. 10 in terms of the blade displacement over two cycles of vibration. Due to this phase-shift and blades vibrating out of phase to each other, the flow disturbances and unsteadiness are amplified. Overall, at a lower Reynolds number, a smaller inflow velocity causes the early and larger flow separation whereas the resistance of the boundary layer separation is increased at a higher Reynolds number. The interaction between the fluid flow at different speeds and the blade oscillation has a significant impact on the behaviour of the unsteady flow by primarily influencing the formation of the flow structures.

Fig. 11 shows the iso-surfaces of the vorticity generated from the vibrating blade with different IBPAs at different Reynolds numbers. The vortex structures are coloured by a function of the flow velocity. This figure highlights the effect of blade motion and vibration phase angles on the flow and the development of flow structures. The flow is highly distorted by the blade vibration and it has a significant impact on the development of vortex structures. The vortex generation is dramatically amplified by the oscillating motion of the blade. The pattern of vortex generation and the size of vortex structures strongly depend on the vibration amplitude and phase angle. As the bending mode is considered for the blade vibration in this study, the blade is fixed at the hub and the blade displacement linearly increases along the span, and the maximum amplitude is observed at the tip near the trailing edge. Due to the nature of the bending mode, the vortex structures are small with some rolling up of the separated shear layer in the blade

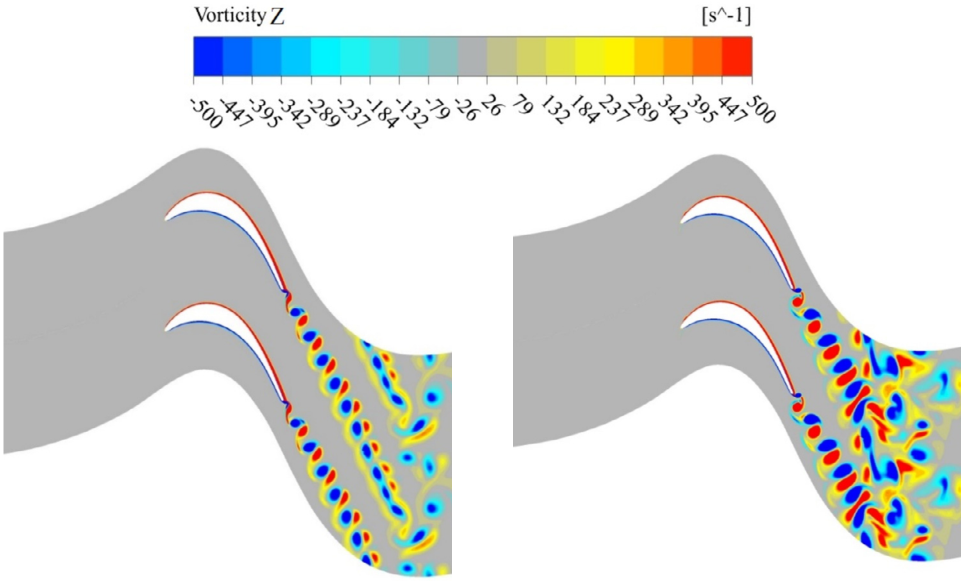

a) 30% Span b) 50% Span

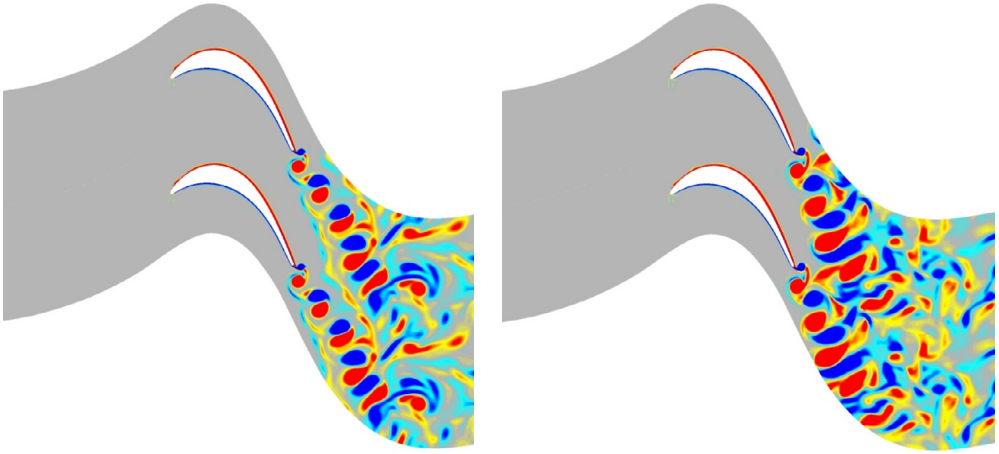

c) 70% Span d) 90% Span

Fig. 15. Instantaneous vorticity contours at different blade span sections at IBPA=0°.

inner region where the vibration amplitude is low, and they become larger as it moves towards the tip along the span. The vortex generation is noticeably high starting from approximately the mid-span section of the blade, and it becomes much more significant in the outer region near the shroud where the vibration amplitude is high. The vortex structures are also much larger in this region. In the case of 0° IBPA, each blade row within the cascade triggers a similar pattern of vortex generation, and the flow structures are mixed up in the downstream region and the wake becomes turbulent. The effect of vibration phase angle on the unsteady flow and flow structures can be clearly seen in the 180° IBPA case. In this case, the blades in a cascade are vibrating out of phase to each other with an angle of 180°. Therefore, the pitch length between two consecutive blades changes in time within a vibration cycle, and it has a great impact on the vortex generation process. Due to this nature, the vortex structures generated from each blade row are highly disturbed by those of the neighbouring blades. This physical behaviour leads to a higher turbulence in the wake region. The effect of blades vibrating out of phase is not just seen in the wake region but also it is noticeable on the blade surfaces. The vortex structures start to develop near the leading edge before it becomes stronger near the trailing edge. In terms of Reynolds number, the flow separation and separation bubbles are observed on the suction surface in both IBPA cases at $\mathrm{Re} = 2.5 \times 10^4$. When $\mathrm{Re} = 5.1 \times 10^4$, a strong flow recirculation can be seen in the flow separation zone at IBPA=180° whereas the flow structures are mostly uniform on the suction surface with some detachment in the blade aft region near the trailing edge at IBPA=0°. Similar flow behaviour is detected at $\mathrm{Re} = 7.5 \times 10^4$; however, the flow structures and recirculation are much larger and stronger at this Reynolds number. The vortex generation is much stronger in the blade outer region near the shroud where the vibration amplitude is large. The downstream wake and turbulence are higher in the 180° IBPA case compared to the 0° IBPA case. As the fluid velocity becomes higher with increasing Reynolds number, it can minimise the separation bubbles and reduce the flow separation. The out-of-phase blade motions between the two consecutive blades, shown in Fig. 10, have a great impact on the formation of the flow structures and the level of turbulence in the downstream flow.

To have a confidence on the accuracy of the flow resolved, the near wall mesh resolution over the blade in each direction for the stationary blade case and one of the vibrating blade cases at $\mathrm{Re} = 7.5 \times 10^4$ and $\mathrm{IBPA} = 180°$ are presented in Fig. 12(a). In this figure, Δn^+ and Δs^+ are the near wall resolution in the directions normal and tangential to the blade, and Δz^+ is the wall resolution in the span-wise direction. It is seen that Δn^+ is much lower than

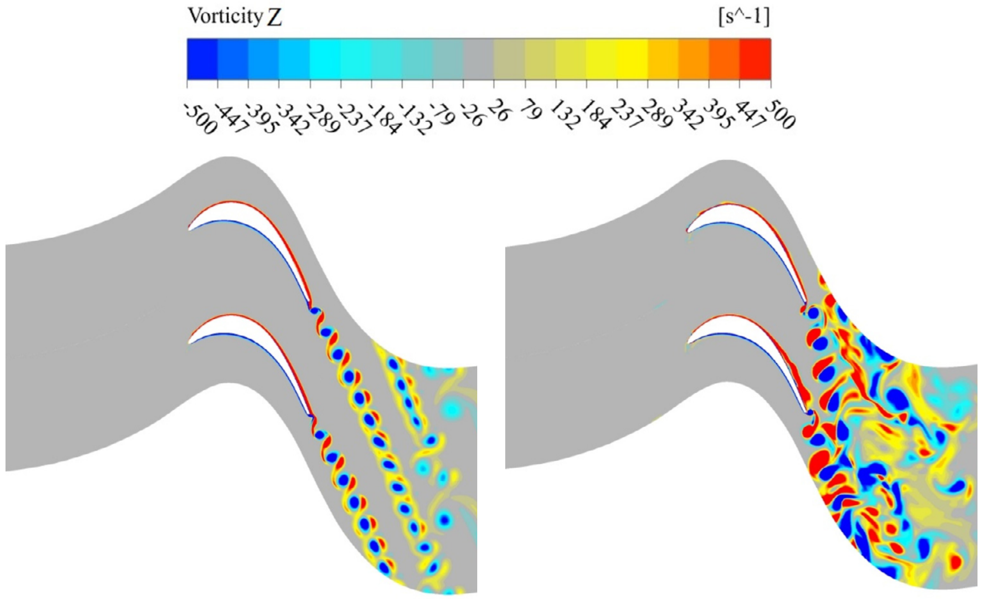

a) 30% Span

b) 50% Span

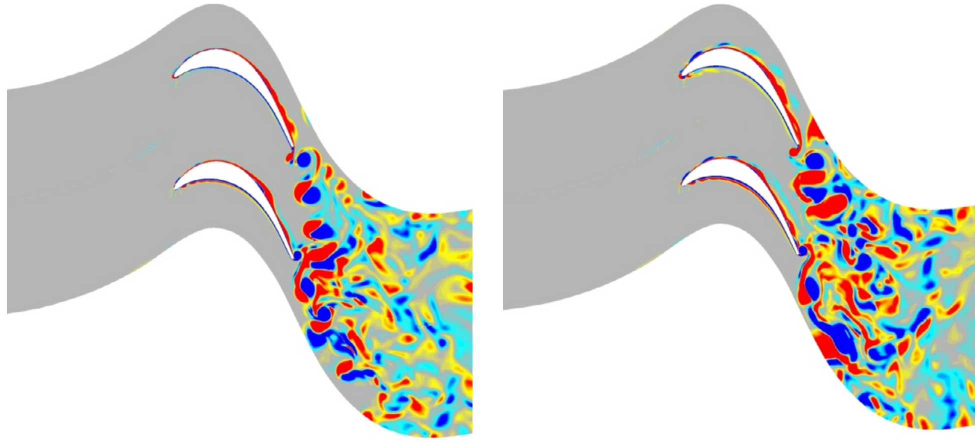

c) 70% Span

d) 90% Span

Fig. 16. Instantaneous vorticity contours at different blade span sections at IBPA=180°.

1, whereas the maximum values of Δs^+ and Δz^+ are lower than 10, which can be considered sufficient for a fully resolved flow. Another important parameter to evaluate whether the turbulent flow structures are precisely resolved over the surface of the LPT blade is the power spectra of the turbulent kinetic energy. The turbulent kinetic energy is calculated by: $TKE = \left(\overline{u'u'} + \overline{v'v'} + \overline{w'w'}\right)/2$, where u', v' and w' are the velocity fluctuations in x, y and z directions, respectively. The power spectra of the kinetic energy (E_k) over both stationary and vibrating LPT blade at Re $= 7.5 \times 10^4$ and IBPA $= 180°$ are provided in Fig. 12(b). The results show that the computed energy spectrum shows a good agreement with the Kolmogorov -5/3 slope line.

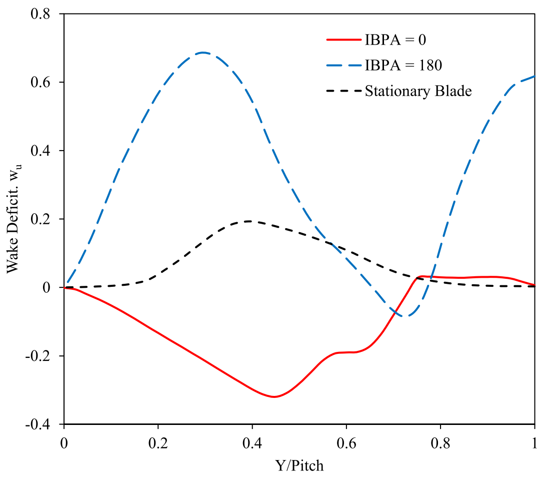

Fig. 17. The effects of vibrations on the wake profile over LPT blade at different IBPAs.

A detailed analysis of the consequences of the blade vibration on the vortex generation process and the downstream wake will now be discussed based on the case at Re $= 5.1 \times 10^4$. Figs. 13–14 illustrate the instantaneous vorticity generation contours after different cycles of vibration at IBPA=0° and 180°. The recirculating flows are generated once the blade starts to oscillate, and the primarily generated vortex flows are pushed back by the newly generated recirculations at both IBPA values. It can be seen in Fig. 13 that for IBPA=0°, periodic flow pattern of the recirculations is generated after different number of vibrations. These vortex generations become noticeable after 10 oscillations, and the separated shear layer from the upper blade interacts with the lower one. The

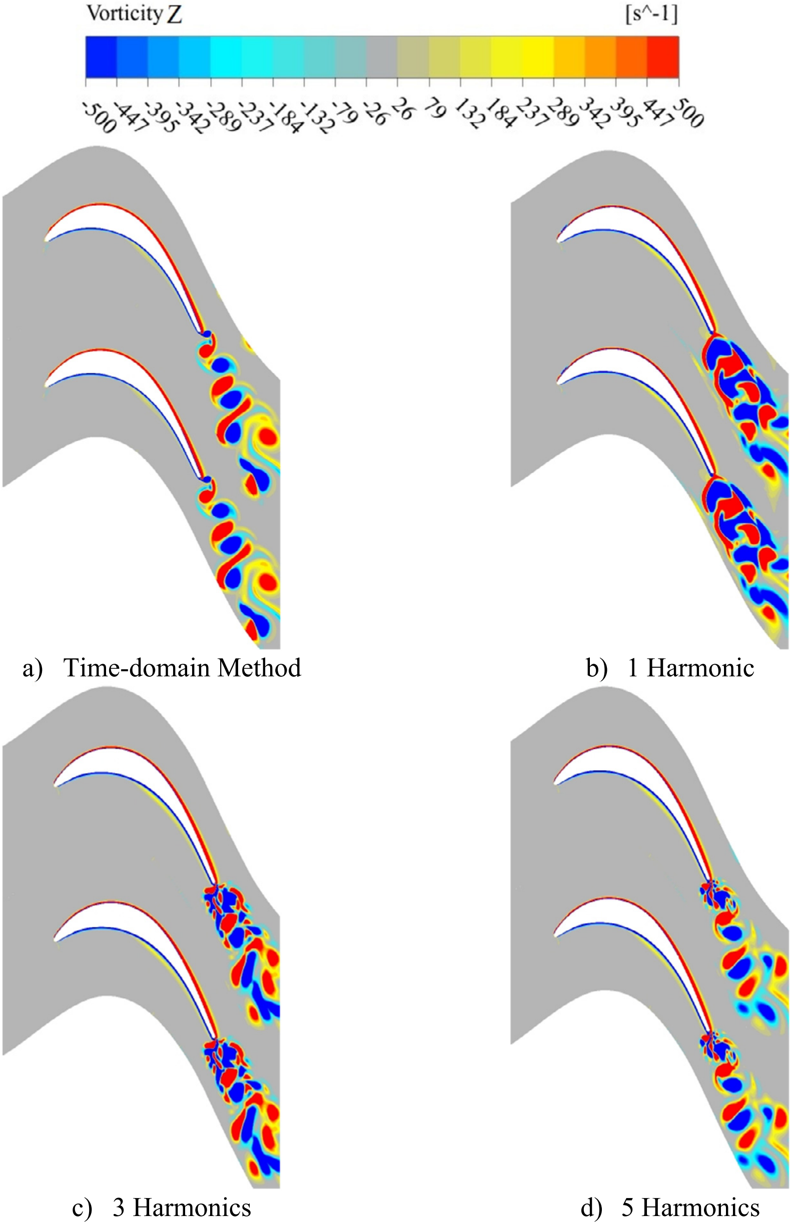

Fig. 18. Comparison of instantaneous vorticity contours between the time-domain method and the harmonic balance method using different harmonics at IBPA=0°.

formation of the separation bubble near the trailing edge of the LPT blades becomes more non-uniform after 15 vibration periods at IBPA=0°. In contrast, these non-uniform vortex generation at IBPA=180°, is more significant even after just five oscillations (see Fig. 14). The rolling up of the recirculations and the separation of the flow are detected on the surface of the LPT blades after 10 vibration periods and it becomes stronger after 15 vibration periods. It can be seen that the size of the rolling up is larger and the flow disturbance is more noticeable after 20 oscillations. At IBPA=180°, the downstream flow and wake is more unsteady and turbulent than that of the IBPA of 0° as the flow structures in the downstream region are highly distorted by those of the neighbouring blades.

The variations of the vorticity contours at various blade sections are presented in Figs. 15–16. The results are provided after 20 oscillation periods to envisage the effects of various oscillation phase-angles on the flow structure over the vibrating blades. It is observed that small and similar flow structures and recirculations are generated at 30% of the span in both IBPA cases. This is because of the small oscillation amplitude at 30% of span and therefore, the inter blade phase angle has a negligible impact. But obvious deviations among the cases are observed at 50% span, and these deviations become noticeable by moving in the span-wise direction at the 70% and 90% span sections. The flow structures from the vortex generation of the upper blade go down and mix with the recirculation generated from the lower blade just after shedding from the trailing edge at IBPA=180°. At the external sections of the blades (50% or higher) for both IBPA=0° and 180°, the fluid combination happens as soon as it sheds from the trailing edge. Besides, the transitional flow structure and turbulent fluctuations of the flow become noticeable at IBPA=180°. Consequently, the LPT oscillations have a huge impact on the transitional flow structure and vortex generation, and the shape of the recirculating flows is highly dependent on the amplitude of the blade oscillation and the value of IBPA between the two consecutive blades.

Fig. 17 further depicts the wake profile variations for the stationary blade, and oscillating LPT blades with IBPA=0° and 180° at Re $= 5.1 \times 10^4$. The results are provided for 40% chord down-

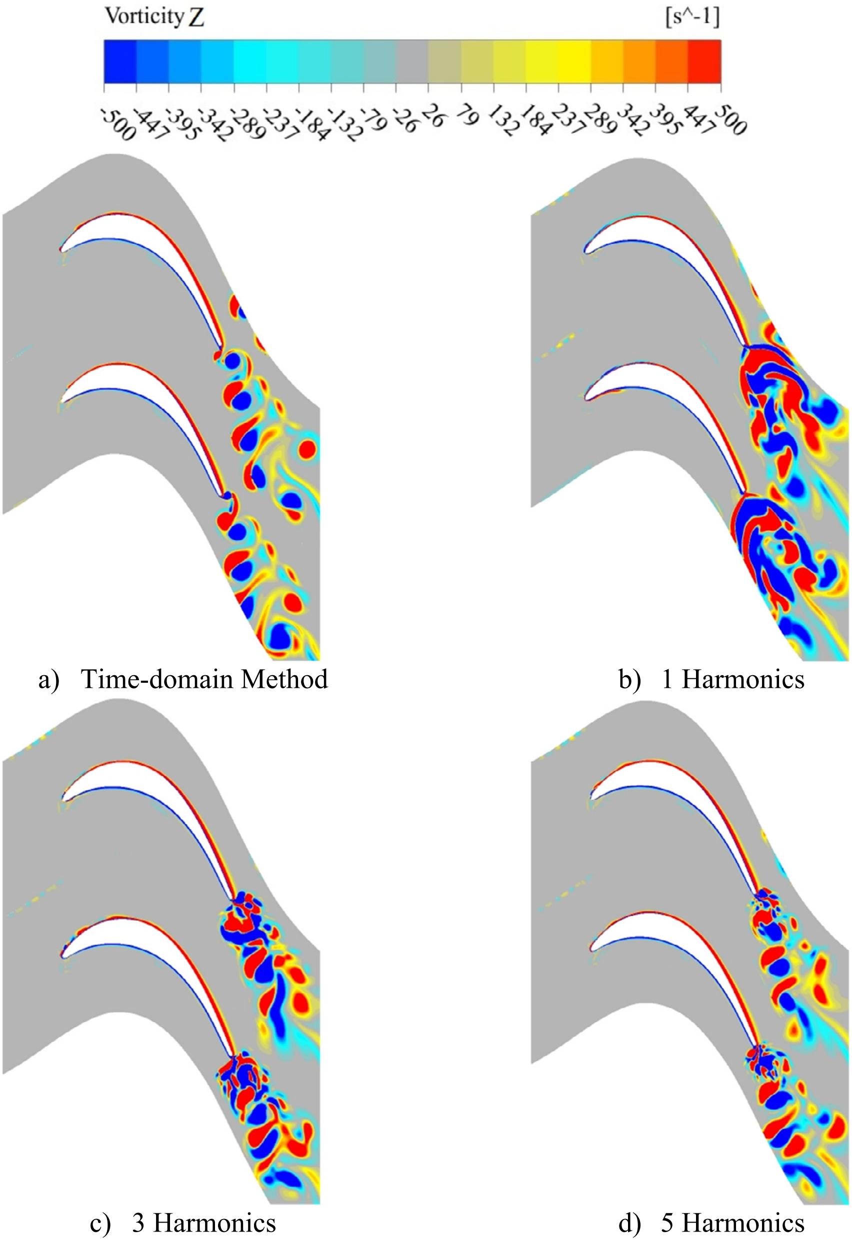

Fig. 19. Comparison of instantaneous vorticity contours between the time-domain method and the harmonic balance method using different harmonics at IBPA=180°.

stream of the trailing edge at the blade mid-span of the lower flow passage. Significant difference is observed for the wake profiles between the stationary and oscillating LPT blades, which indicates that the blades oscillations have significant influence on the transient flow structure around the blades. It can be seen that the vibrations increase the peak value of the wake compared to the stationary LPT blades. The results show that the wake has a transverse profile at IBPA=0° compared to 180°, which has a wavy structure along the pitch direction.

Figs. 18–19 compare the vorticity structures developed from the trailing edge of the blade within the initial periods of vibration at both IBPAs, resolved by the time-domain method and the harmonic balance method using different harmonics. It is observed that the harmonic balance method using one and three harmonics cannot resolve the vortex structures accurately whereas the downstream flow structures computed using 5 harmonics are similar to that of the time-domain solution. However, it is also noticed that the flow structures leaving from the trailing edge of the blade are not accurately resolved even in the case of using five harmonics. This can be noted as the limitation of the harmonic balance method. Nonetheless, it can be concluded that at least 5 harmonics are required to predict the vortex structures due to the effect of the blade flutter with different IBPAs in an LPT if the harmonic balance method is used.

Further comparisons between a DNS model and a standard URANS model are also provided in this paper to highlight the difference between the two models in resolving the unsteady flow. The unsteady pressure coefficient and phase angle at different span sections are compared and presented in Figs. 20–21. The results are extracted at 30% and 90% of span. The results illustrate that the unsteady pressure distribution predicted by the URANS model is reasonably comparable to the DNS model. The aero-damping parameter is one of the critical parameters in the design of aero-engine and low-pressure turbines. This parameter is defined as the total work done by the turbine blades on the air flow during an oscillation period. The aerodynamic work can be defined as:

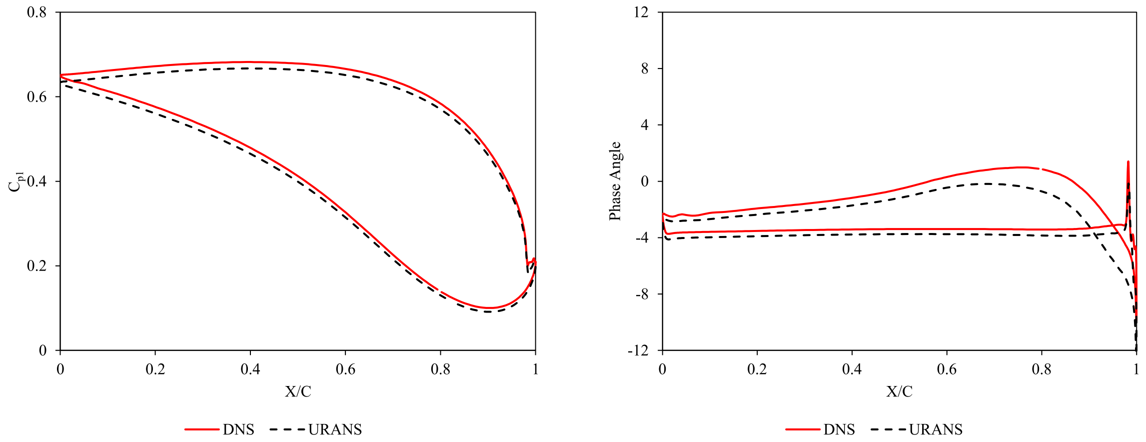

a) C_{p1} at 30% Span b) ϕ at 30% Span

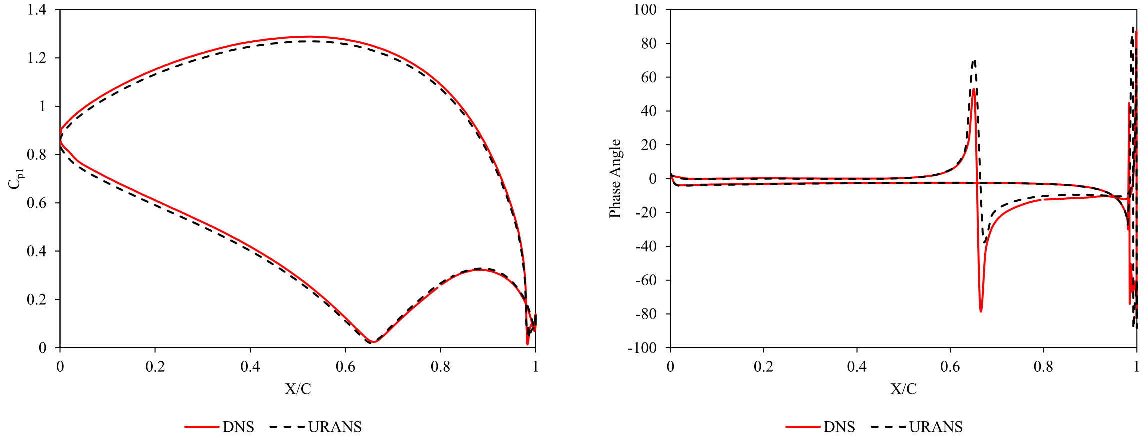

c) C_{p1} at 90% Span d) ϕ at 90% Span

Fig. 20. Unsteady Pressure coefficient (C_{p1}) and phase angle (ϕ) over the oscillating turbine blade at IBPA=0° and Re $= 5.1 \times 10^4$.

$$W = \int_{t_0}^{t_0+T_{period}} \int_{A} p\vec{v}.\hat{n}dAdt \tag{11}$$

In which, t_0, T_{Period}, p and $\vec{v}$ are the initial solution time, time period of the oscillation cycle, flow pressure, and velocity vector of the blade owing to the displacements, respectively. Physically, if the aero-damping parameter is positive, the oscillations are damped for the selected frequency and amplitude. Table 2 shows the values of aero-damping in the Log-Dec format for IBPA=0° and 180°. The results are calculated from both DNS and URANS models. Good agreement is observed between the results of the two models. The results indicate that the URANS model predicts unsteady pressure distribution on the blade surface adequately subject to a clean and uniform inflow condition. Realistically, the inflow condition is not always steady and uniform, especially in a multi-stage turbine where the effects from different blade rows and neighbouring blades are complex and significant. In fact, a dramatic difference is observed between the two models in resolving the downstream wake as shown in Fig. 22. As expected, the URANS model is unable to predict the unsteady and turbulent nature of the flow. The similar behaviour was also discussed in [27]. The inadequacy of resolving the downstream wake leads to a black-box effect and inaccuracy in predicting the aeroelasticity behaviour of the blades when multiple blade row configurations are involved. Employing a high-fidelity numerical model will make it possible to capture the necessary unsteady behaviour of the flow and thereby increasing the accuracy in predicting the flutter behaviour in all blade rows, especially in a multiple blade row configuration.

Table 2
The Aero-damping parameters over the LPT blade at different IBPAs.

Case	DNS	URANS
IBPA=0°	0.027	0.021
IBPA=180°	0.053	0.045

Table 3
Computation times of each numerical model used in the present study.

Methodology	CPU cores	Calculation time
Time-domain method	224	570 hours
Harmonic balance method (one harmonic)	32	15 hours
Harmonic balance method (three harmonic)	32	33 hours
Harmonic balance method (five harmonic)	32	60 hours

The numerical analyses presented in this study were performed on Oswald HPC cluster at Northumbria University. Each node contains Dual Intel Xeon E5-2680 with 128 GB of memory. Total of 224 cores were utilized for the time domain method while 32 cores were only useable for the harmonic balance method as a considerable amount of memory was required for the simulations, which can be noted as the limitation of the harmonic balance method. The details of the computation times for various solution methods are provided in Table 3. It should be pointed out that the required memory for the harmonic balance method is much higher

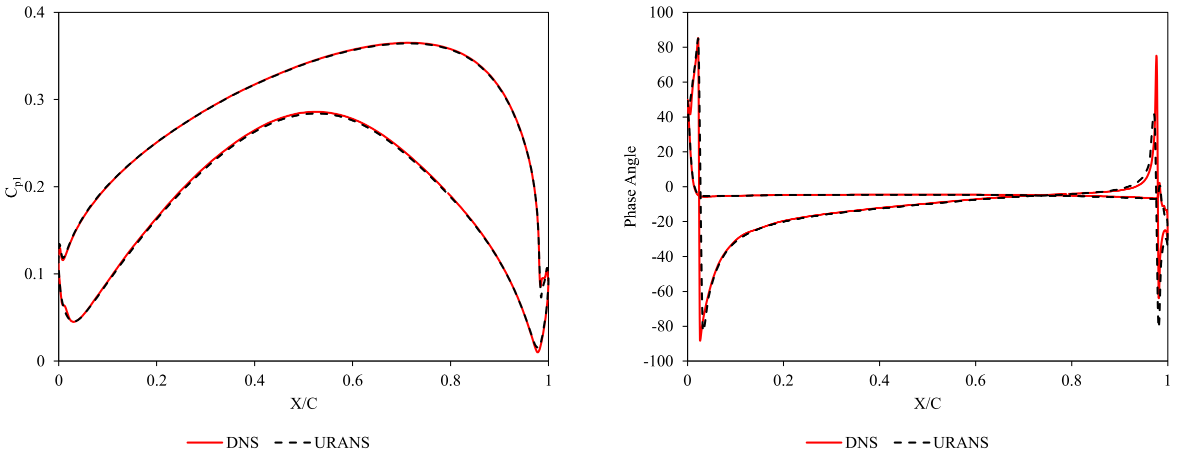

a) C_{p1} at 30% Span

b) ϕ at 30% Span

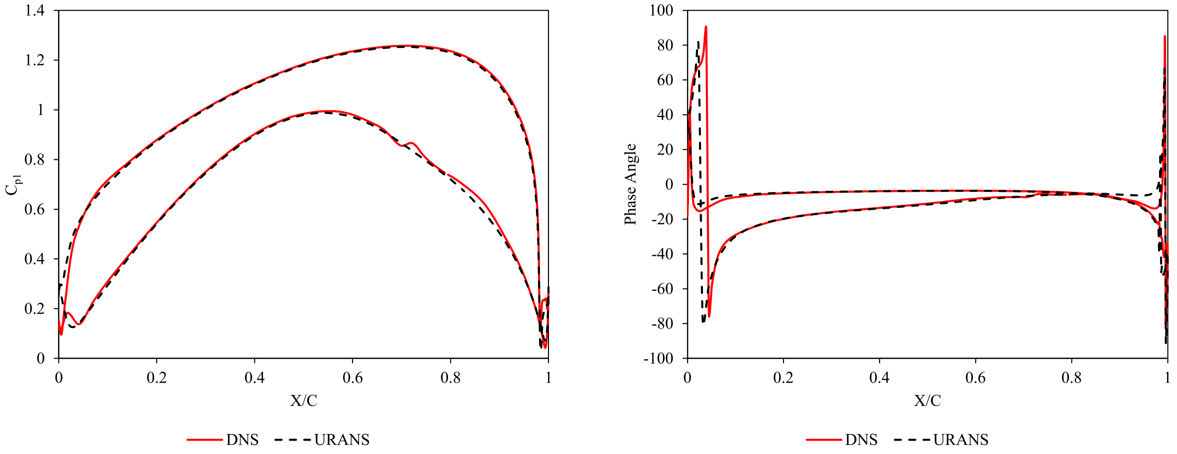

c) C_{p1} at 90% Span

d) ϕ at 90% Span

Fig. 21. Unsteady Pressure coefficient and phase angle over the oscillating turbine blade at IBPA=180° and Re $= 5.1 \times 10^4$.

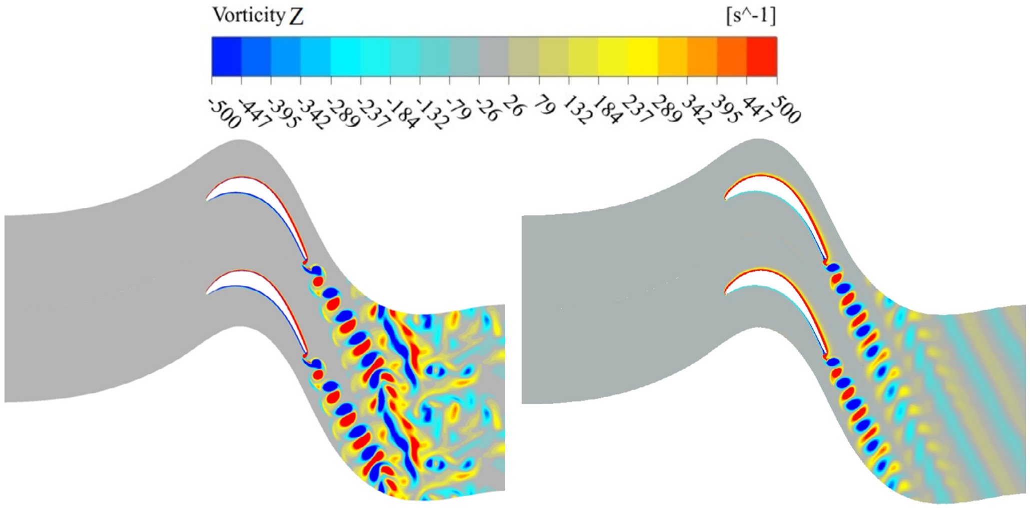

a) DNS Model

b) URANS Model

Fig. 22. Vorticity contours resolved by DNS and URANS models.

compared to the time-domain method. However, the computation time is reduced by 78% by using the harmonic balance method. Besides, the accuracy of this method to predict the aeroelasticity parameters and the impact of the blade's oscillations on the vortex generation process in an LPT is high.

4. Conclusion

In the present study, direct numerical simulations have been performed over oscillating blades in the modern low-pressure turbines to investigate the flutter instabilities and transitional flow structures due to the oscillations of the blades. Previous studies only concentrated on the stationary LPT blades. However, it is essential to consider the realistic oscillations of the LPT blades to have more accurate predictions. Therefore, in this study, a high-fidelity computational model is developed based on a DNS method to capture the unsteady flow behaviour and pressure fluctuations over the blades of the modern aeroengine turbines. The simulations were performed at two different IBPAs in the T016A turbine.

Firstly, the numerical results were compared to the experiment and reference simulations, and an excellent agreement was observed between the present simulation and the reference data. Then, the time-averaged pressure coefficient over the turbine blades were investigated over both stationary and oscillating blades. Considerable deviation was observed for the C_p over the suction side of blade between the oscillating LPT blade and the stationary one. It was concluded that the oscillations have significant impact on the vortex generation process and recirculation flows in the separated shear layer over the blade surface, that is directly related to the location of the separation point over the blade surface. The obtained numerical results revealed that the impact of the vibrations on the flow structures is much higher at the blade tips due to the higher vibration amplitudes.

For IBPA=0°, a wavy pattern of vortex generation was detected together with more fluid mixing in the downstream region of the oscillating blades. But, for IBPA=180°, the structures of the fluid flow generated by the superior blade have a great impact on the lower one by mixing with the recirculation and vortex generation from the lower blade in the wake region just after shedding from the trailing edge. It is concluded that the flow instabilities and perturbations are stronger over the external surface of the blade for both IBPA=0° and 180°. Moreover, the aerodynamic damping parameters are positive for all of the test cases, but they are greater at higher values of the inter blade phase angle. In addition, the vortex generation is much stronger in the blade outer region near the shroud where the vibration amplitude is large. The downstream wake and turbulence are higher in the 180° IBPA case compared to the 0° IBPA case. Raising Reynolds number can minimise the separation bubbles in the separation zone and can reduce the size of flow separation. The differences of pressure distribution on the aerofoil surfaces between both IBPA cases can be reduced by raising Reynolds number. However, the differences are still considerable in the blade outer region due to the high amplitude of oscillation near the blade tip. An accurate prediction of the flow behaviour over the blade surface subject to a relatively large amplitude of vibration will make it possible to enhance the physical understanding of the blade flutter and thereby overcoming the aeroelastic instabilities as well as ensuring the structural integrity of the blade.

Apart from the time-domain method, a harmonic balance method is also employed in the present study, and it is found that at least 5 harmonics are required to resolve the flow structures. However, the harmonic balance method requires a significant amount of memory compared to the standard time domain method. The unsteady pressure coefficient (C_{p1}), and the pressure phase angle (ϕ) over the LPT blades have been evaluated using DNS and URANS models, and they reasonably agree well with each other. However, the URANS model is unable to resolve the downstream wake and flow behaviour leading to an underestimation of the turbulence and unsteadiness in the downstream flow. Overall, employing a high-fidelity numerical model makes it possible to capture the necessary unsteady behaviour of the flow and thereby increasing the accuracy in predicting the flutter behaviour of the blades, especially in a multiple blade row configuration. The important flow structures due to a bending mode of the blade vibration, where the amplitude is not constant along the blade span, cannot be obtained using 2D or quasi-3D models. This study provides a comprehensive understanding of flow structures associated with a 3D blade structure and 3D vibration mode.

Declaration of competing interest

The authors declare that they have no known competing financial interests or personal relationships that could have appeared to influence the work reported in this paper.

Acknowledgements

The authors would like to acknowledge the financial support received from the Engineering Physics and Science Research Council of the UK (EPSRC EP/R010633/1).

References

[1] C. Sun, B. Wang, Y. Liu, X. Wang, C. Li, H. Wang, J. Tan, Design of high accuracy cylindrical profile measurement model for low-pressure turbine shaft of aero engine, Aerosp. Sci. Technol. 95 (2019) 105442.

[2] C.G. Himmel, Ultra-High Lift Blades for Low Pressure Turbines, University of Cambridge, 2010.

[3] H.P. Hodson, R.J. Howell, Bladerow interactions, transition, and high-lift aerofoils in low-pressure turbines, Annu. Rev. Fluid Mech. 37 (2005) 71–98.

[4] J.D. Coull, H.P. Hodson, Unsteady boundary-layer transition in low-pressure turbines, J. Fluid Mech. 681 (2011) 370–410.

[5] J. Panovsky, R.E. Kielb, A design method to prevent low pressure turbine blade flutter, J. Eng. Gas Turbines Power 122 (1999) 89–98.

[6] J.J. Waite, R.E. Kielb, Physical understanding and sensitivities of low pressure turbine flutter, J. Eng. Gas Turbines Power 137 (2014).

[7] J.J. Waite, R.E. Kielb, The impact of blade loading and unsteady pressure bifurcations on low-pressure turbine flutter boundaries, J. Turbomach. 138 (2015).

[8] R. Corral, A. Vega, The low reduced frequency limit of vibrating airfoils—Part I: theoretical analysis, J. Turbomach. 138 (2015).

[9] E.H. Dowell, A Modern Course in Aeroelasticity, Springer International Publishing, Cham, 2015.

[10] X. Dong, Y. Zhang, Y. Zhang, Z. Zhang, X. Lu, Numerical simulations of flutter mechanism for high-speed wide-chord transonic fan, Aerosp. Sci. Technol. 105 (2020) 106009.

[11] J. Ren, H. Huang, D. Wang, X. Dong, B. Cao, An efficient coupled-mode flutter analysis method for turbomachinery, Aerosp. Sci. Technol. 106 (2020) 106215.

[12] T.H. Nguyen, P.T. Nguyen, F. Garnier, Evaluation of the relationship between the aerothermodynamic process and operational parameters in the high-pressure turbine of an aircraft engine, Aerosp. Sci. Technol. 86 (2019) 93–105.

[13] W. Ning, L. He, Computation of unsteady flows around oscillating blades using linear and nonlinear harmonic Euler methods, J. Turbomach. 120 (1998) 508–514.

[14] K.C. Hall, C.B. Lorence, Calculation of three-dimensional unsteady flows in turbomachinery using the linearized harmonic Euler equations, J. Turbomach. 115 (1993) 800–809.

[15] D. Wang, X. Huang, A complete rotor–stator coupling method for frequency domain analysis of turbomachinery unsteady flow, Aerosp. Sci. Technol. 70 (2017) 367–377.

[16] L. He, Harmonic solution of unsteady flow around blades with separation, AIAA J. 46 (2008) 1299–1307.

[17] M.T. Rahmati, L. He, Y.S. Li, The blade profile orientations effects on the aeromechanics of multirow turbomachines, J. Eng. Gas Turbines Power 138 (2015) 062606.

[18] M.T. Rahmati, L. He, D.X. Wang, Y.S. Li, R.G. Wells, S.K. Krishnababu, Nonlinear time and frequency domain methods for multirow aeromechanical analysis, J. Turbomach. 136 (2013) 041010.

[19] S. Win Naung, M. Rahmati, H. Farokhi, Aerodynamic analysis of a wind turbine with elevated inflow turbulence and wake using harmonic method, in: ASME 2019 38th International Conference on Ocean, Offshore and Arctic Engineering, 2019.

[20] S. Win Naung, M. Rahmati, H. Farokhi, Aeromechanical analysis of wind turbines using non-linear harmonic method, in: ASME 2019 38th International Conference on Ocean, Offshore and Arctic Engineering, 2019.

[21] S. Win Naung, M. Rahmati, H. Farokhi, Nonlinear frequency domain solution method for aerodynamic and aeromechanical analysis of wind turbines, Renew. Energy 167 (2021) 66–81.

[22] S. Win Naung, M. Rahmati, H. Farokhi, Aeromechanical analysis of a complete wind turbine using nonlinear frequency domain solution method, J. Eng. Gas Turbines Power 143 (2021) 011018.

[23] P.G. Tucker, Computation of Unsteady Internal Flows, Springer US, 2001.

[24] P.G. Tucker, Computation of unsteady turbomachinery flows: Part 1—progress and challenges, Prog. Aerosp. Sci. 47 (2011) 522–545.
[25] P.G. Tucker, Unsteady Computational Fluid Dynamics in Aeronautics, Springer Netherlands, 2014.
[26] M.E. Nakhchi, S. Win Naung, M. Rahmati, DNS of secondary flows over oscillating low-pressure turbine using spectral/hp element method, Int. J. Heat Fluid Flow 86 (2020) 108684.
[27] S. Win Naung, M. Rahmati, H. Farokhi, Direct numerical simulation of interaction between transient flow and blade structure in a modern low-pressure turbine, Int. J. Mech. Sci. 192 (2021) 106104.
[28] X.Q. Huang, L. He, D.L. Bell, Experimental and computational study of oscillating turbine cascade and influence of part-span shrouds, J. Fluids Eng. 131 (2009).
[29] P. Stadtmüller, Investigation of wake-induced transition on the LP turbine cascade T106A-EIZ, DFG-Verbundprojekt Fo, 136, 2001.
[30] Y. Wang, F. Chen, H. Liu, H. Chen, Large eddy simulation of unsteady transitional flow on the low-pressure turbine blade, Sci. China, Technol. Sci. 57 (2014) 1761–1768.
[31] A. Garai, L.T. Diosady, S.M. Murman, N.K. Madavan, DNS of low-pressure turbine cascade flows with elevated inflow turbulence using a discontinuous-Galerkin spectral-element method, in: ASME Turbo Expo 2016: Turbomachinery Technical Conference and Exposition, 2016.
[32] J.G. Wissink, DNS of separating, low Reynolds number flow in a turbine cascade with incoming wakes, Int. J. Heat Fluid Flow 24 (2003) 626–635.
[33] J.G. Wissink, W. Rodi, Direct numerical simulations of transitional flow in turbomachinery, J. Turbomach. 128 (2006) 668–678.
[34] V. Michelassi, J. Wissink, W. Rodi, Analysis of DNS and LES of flow in a low pressure turbine cascade with incoming wakes and comparison with experiments, Flow Turbul. Combust. 69 (2002) 295–329.
[35] R. Ranjan, S.M. Deshpande, R. Narasimha, New insights from high-resolution compressible DNS studies on an LPT blade boundary layer, Comput. Fluids 153 (2017) 49–60.
[36] R.D. Sandberg, V. Michelassi, R. Pichler, L. Chen, R. Johnstone, Compressible direct numerical simulation of low-pressure turbines—Part I: methodology, J. Turbomach. 137 (2015).
[37] V. Michelassi, L.-W. Chen, R. Pichler, R.D. Sandberg, Compressible direct numerical simulation of low-pressure turbines—Part II: effect of inflow disturbances, J. Turbomach. 137 (2015).
[38] M.M. Opoka, H.P. Hodson, Transition on the T106 LP turbine blade in the presence of moving upstream wakes and downstream potential fields, J. Turbomach. 130 (2008).
[39] A. Mahallati, S.A. Sjolander, Aerodynamics of a low-pressure turbine airfoil at low Reynolds numbers—Part II: blade-wake interaction, J. Turbomach. 135 (2012).
[40] A. Daniel Antony, M. Gopalsamy, C.B.V. Viswanadh, R. Krishnaraj, Structural dynamic analysis of turbine blade, IOP Conf. Ser., Mater. Sci. Eng. 247 (2017) 012007.
[41] G.L. Forbes, R.B. Randall, Estimation of turbine blade natural frequencies from casing pressure and vibration measurements, Mech. Syst. Signal Process. 36 (2013) 549–561.
[42] D.H. Wacks, M.E. Nakhchi, M. Rahmati, Forced response of a low-pressure turbine blade using spectral/hp element method: direct numerical simulation, J. Appl. Comput. Mech. 7 (2021) 135–147.
[43] C.H. Sieverding, D. Ottolia, C. Bagnera, A. Comadoro, J.-F. Brouckaert, J.-M. Desse, Unsteady turbine blade wake characteristics, J. Turbomach. 126 (2004) 551–559.
[44] Z. Wei, M. Ni, X. Gan, W. Chen, P. Chen, Generation of unsteady incoming wakes for wake/blade interaction, Aerosp. Sci. Technol. 106 (2020) 106127.